J|A|C|S ARTICLES

Published on Web 03/16/2009

Strong H···F Hydrogen Bonds as Synthons in Polymeric Quantum Magnets: Structural, Magnetic, and Theoretical Characterization of $[Cu(HF_2)(pyrazine)_2]SbF_6$, $[Cu_2F(HF)(HF_2)(pyrazine)_4](SbF_6)_2$, and $[CuAg(H_3F_4)(pyrazine)_5](SbF_6)_2$

Jamie L. Manson,*[,†] John A. Schlueter,[‡] Kylee A. Funk,[‡] Heather I. Southerland,[†] Brendan Twamley,[§] Tom Lancaster,[||] Stephen J. Blundell,[||] Peter J. Baker,[||] Francis L. Pratt,[⊥] John Singleton,[#] Ross D. McDonald,[#] Paul A. Goddard,[||] Pinaki Sengupta,[#,▽] Cristian D. Batista,[▽] Letian Ding,[○] Changhoon Lee,[◆] Myung-Hwan Whangbo,[◆] Isabel Franke,[||] Susan Cox,[#] Chris Baines,[¶] and Derek Trial[†]

Department of Chemistry and Biochemistry, Eastern Washington University, Cheney, Washington 99004, Materials Science Division, Argonne National Laboratory, Argonne, Illinois 60439, University Research Office, University of Idaho, Moscow, Idaho 83844, Clarendon Laboratory, Department of Physics, Oxford University, Oxford, U.K. OX1 3PU, ISIS Pulsed Muon Facility, Rutherford-Appleton Laboratory, Chilton, Oxfordshire, U.K. OX11 0QX, National High Magnetic Field Laboratory and Theoretical Division, Los Alamos National Laboratory, Los Alamos, New Mexico 87545, Department of Physics and Astronomy, University of Southern California, Los Angeles, California 90089, Department of Chemistry, North Carolina State University, Raleigh, North Carolina 27695, and Swiss Muon Source (SμS), Paul Scherrer Institute, CH-5253 Villigen, Switzerland

Received November 14, 2008; E-mail: jmanson@ewu.edu

Abstract: Three Cu^{2+}-containing coordination polymers were synthesized and characterized by experimental (X-ray diffraction, magnetic susceptibility, pulsed-field magnetization, heat capacity, and muon-spin relaxation) and electronic structure studies (quantum Monte Carlo simulations and density functional theory calculations). $[Cu(HF_2)(pyz)_2]SbF_6$ (pyz = pyrazine) (**1a**), $[Cu_2F(HF)(HF_2)(pyz)_4](SbF_6)_2$ (**1b**), and $[CuAg(H_3F_4)(pyz)_5](SbF_6)_2$ (**2**) crystallize in either tetragonal or orthorhombic space groups; their structures consist of 2D square layers of $[M(pyz)_2]^{n+}$ that are linked in the third dimension by either HF_2^- (**1a** and **1b**) or $H_3F_4^-$ (**2**). The resulting 3D frameworks contain charge-balancing SbF_6^- anions in every void. Compound **1b** is a defective polymorph of **1a**, with the difference being that 50% of the HF_2^- links are broken in the former, which leads to a cooperative Jahn−Teller distortion and $d_{x^2-y^2}$ orbital ordering. Magnetic data for **1a** and **1b** reveal broad maxima in χ at 12.5 and 2.6 K and long-range magnetic order below 4.3 and 1.7 K, respectively, while **2** displays negligible spin interactions owing to long and disrupted superexchange pathways. The isothermal magnetization, $M(B)$, for **1a** and **1b** measured at 0.5 K reveals contrasting behaviors: **1a** exhibits a concave shape as B increases to a saturation field, B_c, of 37.6 T, whereas **1b** presents an unusual two-step saturation in which $M(B)$ is convex until it reaches a step near 10.8 T and then becomes concave until saturation is reached at 15.8 T. The step occurs at two-thirds of M_{sat}, suggesting the presence of a ferrimagnetic structure. Compound **2** shows unusual hysteresis in $M(B)$ at low temperature, although χ vs T does not reveal the presence of a magnetic phase transition. Quantum Monte Carlo simulations based on an anisotropic cubic lattice were applied to the magnetic data of **1a** to afford $g = 2.14$, $J = -13.4$ K (Cu-pyz-Cu), and $J_\perp = -0.20$ K (Cu−F···H···F−Cu), while χ vs T for **1b** could be well reproduced by a spin-1/2 Heisenberg uniform chain model for $g = 2.127(1)$, $J_1 = -3.81(1)$, and $zJ_2 = -0.48(1)$ K, where J_1 and J_2 are the intra- and interchain exchange couplings, respectively, which considers the number of magnetic nearest-neighbors (z). The $M(B)$ data for **1b** could not be satisfactorily explained by the chain model, suggesting a more complex magnetic structure in the ordered state and the need for additional terms in the spin Hamiltonian. The observed variation in magnetic behaviors is driven by differences in the H···F hydrogen-bonding motifs.

1. Introduction

In recent years, many synthetic strategies have emerged with regard to the crystal engineering of functional magnetic materials that exhibit cooperative properties such as long-range magnetic ordering, spin crossover, and magnetic bistability.[1] The main

[†] Eastern Washington University.
[‡] Argonne National Laboratory.
[§] University of Idaho.
[||] Oxford University.
[⊥] Rutherford-Appleton Laboratory.
[#] National High Magnetic Field Laboratory, LANL.
[▽] Theoretical Division, LANL.
[○] University of Southern California.
[◆] North Carolina State University.
[¶] Paul Scherrer Institute.

10.1021/ja808761d CCC: $40.75

goal of chemists working in this area is the targeted design of such materials through the self-assembly of appropriate molecular building blocks (synthons) where the metal ion and/or organic components bear magnetic moments. Among the various design options available to chemists are coordinate covalent interactions between (transition, lanthanide, or actinide) metal ions and the organic donor ligands, with such interactions generally providing very robust coordination complexes or polymers. A soft chemical approach that offers greater flexibility to organize synthons into patterned networks is the use of hydrogen bonding. By exploiting these relatively weak intermolecular interactions, lattice (and spin) dimensionality, molecular positioning, and parameters such as exchange coupling constants (J_1, J_2, etc.) and long-range magnetic ordering temperatures (T_c or T_N) can be readily tuned. Unfortunately, the ability to predict the ensuing structure and its physical properties remains a difficult challenge.

The bifluoride ion, HF_2^-, is a small molecule that has yet to be realized as a synthon in crystal engineering; thus, very little is known about its ligand properties or chemical stability. Our interest in bifluoride ion stems from the desire to employ strong hydrogen bonds as scaffolds and magnetic exchange mediators in molecular and polymeric structures. Recent theoretical studies on D_{2h}-symmetric HF_2^- have concluded that its H···F bonds are indeed the strongest known hydrogen bonds, with a calculated bond enthalpy of 175 kJ/mol.[2] Notably, the strength of these H···F bonds greatly exceeds the donor−acceptor type of interactions found in the solid forms of hydrofluoric acid (H−F···H−F; 29 kJ/mol) and water (O−H···O−H; 20 kJ/mol).[3]

In addition to the K^+ and NH_4^+ salts of HF_2^- that have long been known,[4] bifluoride salts with organic cations such as pyridinium,[5] *p*-toluidinium,[6] diisopropylammonium[7] and *L*-argininium[8] have also been structurally characterized. The only reported paramagnetic coordination compounds are $[pipzH_2][MnF_4(HF_2)]$ (pipz = piperazine)[9] and $[Cu(HF_2)(pyz)_2]BF_4$[10] (pyz = pyrazine), which contain Mn^{3+} ($S = 2$) and Cu^{2+} ($S = 1/2$) ions, respectively. The Mn-compound shows negligible magnetic coupling, while $[Cu(HF_2)(pyz)_2]BF_4$ does indeed exhibit long-range magnetic order (LRO) below 1.54 K.[10] The weak superexchange reported for $[pipzH_2][MnF_4(HF_2)]$ is apparently a consequence of the low Mn−F···H bond angle of 111.7°.[9] These latter compounds possess symmetric H···F bonds. The ability of HF_2^- to efficiently mediate magnetic interactions is open to question, and the lack of suitable model systems renders the possibility worthy of further investigation.

Bifluoride is the smallest and most common adduct of HF, but in a few cases $H_2F_3^-$ and $H_3F_4^-$ can also exist in the solid state.[11,12] For instance, some of us recently reported the structural and vibrational properties of the complex transition metal salt $[Cu(dpd)_2](H_2F_3)_2$ (dpd = di-2-pyridyl-methanediol), which contains $H_2F_3^-$ anions in pseudo-C_{2v} symmetry.[11a] The overall symmetry of the molecule can be best described as an asymmetric, hydrogen-bonded HF_2^-/HF adduct, but a less distorted $H_2F_3^-$ molecule has been shown to exist in the tetramethylammonium salt;[11b] crystal packing forces may influence the resulting molecular geometry. Because there are few examples to examine, even less is known about the $H_3F_4^-$ ion, which is relatively less stable than $H_2F_3^-$ or HF_2^-.[11c,12] For a homologous series of HF adducts, the increasing size of the molecule progressively leads to decreased chemical stability. X-ray diffraction and IR structural studies of KH_3F_4 revealed a centrally located fluoride ion (with C_{3v} symmetry) surrounded by three hydrogen-bonded HF molecules.[12] Furthermore, HF adducts tend to dissociate in aqueous solution, which renders them difficult to use as potential ligands in coordination chemistry. Clearly, more compounds are required to further our understanding of the interactions in these highly unusual molecules.

Our goal is to utilize HF_2^- and other HF adducts as synthons much like CN^-, N_3^-, NCS^-, NCO^-, and others.[13−16] To this end, we have synthesized and characterized three novel three-dimensional (3D) coordination polymers that contain Cu^{2+} ions: $[Cu(HF_2)(pyz)_2]SbF_6$ (**1a**), $[Cu_2F(HF)(HF_2)(pyz)_4](SbF_6)_2$ (**1b**), and $[CuAg(H_3F_4)(pyz)_5](SbF_6)_2$ (**2**). Both **1a** and **1b** possess the desired $\mu_{1,3}$-HF_2^- bridges, hence demonstrating the coordination versatility of the HF_2^- anion, while **2** is the first compound to possess bridging $H_3F_4^-$ ions. Herein, we describe the structural and magnetic properties of **1a**, **1b**, and **2** and show that HF adducts are stable and potential synthons in the targeted design of magnetic coordination polymers that exhibit a range of lattice and spin dimensionalities. In order to better understand the bulk magnetic behaviors of **1a** and **1b**, we combined our experimental

(1) *Magnetism: Molecules to Materials*, Vols. 1−5; Miller, J. S., Drillon, M., Eds.; Wiley-VCH: Weinheim, 2002−2006, and references therein.
(2) Pendas, A. M.; Blanco, M. A.; Francisco, E. *J. Chem. Phys.* **2006**, *125*, 184112.
(3) Jeffrey, G. A. *An Introduction to Hydrogen Bonding*; Oxford University Press: New York, 1997; pp 33−39.
(4) (a) Peterson, S. W.; Levy, H. A. *J. Chem. Phys.* **1952**, *20*, 704. (b) Troyanov, S. I. *Crystallogr. Rep.* **2005**, *50*, 773.
(5) Boenigk, D.; Mootz, D. *J. Am. Chem. Soc.* **1988**, *110*, 2135.
(6) Williams, J. M.; Schneemeyer, L. F. *J. Am. Chem. Soc.* **1973**, *95*, 5780.
(7) Reiss, G. J. *Acta Crystallogr.* **2001**, *C57*, 994.
(8) Ramos Silva, M.; Paixao, J. A.; Matos Beja, A.; Alte da Veiga, L. *Acta Crystallogr.* **2000**, *C56*, 104.
(9) Bentrup, U.; Harms, K.; Massa, W.; Pebler, J. *Solid State Sci.* **2000**, *2*, 373.
(10) Manson, J. L.; Conner, M. M.; Schlueter, J. A.; Lancaster, T.; Blundell, S. J.; Brooks, M. L.; Pratt, F. L.; Papageorgiou, T.; Bianchi, A. D.; Wosnitza, J.; Whangbo, M.-H. *Chem. Commun.* **2006**, 4894.
(11) (a) Manson, J. L.; Southerland, H. I.; Twamley, B.; Rai, R.; Musfeldt, J. L. *Dalton Trans.* **2007**, 5655. (b) Troyanov, S. I.; Morozov, I. V.; Kemnitz, E. *Z. Anorg. Allg. Chem.* **2005**, *631*, 1651. (c) Boenigk, D.; Mootz, D. *Z. Kristallogr.* **1985**, *170*, 16. (d) Mathieson, T.; Schier, A.; Schmidbaur, H. *Z. Naturforsch, B: Chem. Sci.* **2000**, *55*, 1000. (e) Bourosh, P. N.; Bologa, O. A.; Simonov, Y. A.; Bocelli, G.; Gerbeleu, N. V. *Koord. Khim. (Russ.) Coord. Chem.* **2005**, *31*, 677. (f) Fernandez, F. J.; Alfonso, M.; Schmalle, H. W.; Berke, H. *Organometallics* **2001**, *20*, 3122.
(12) (a) Boenigk, D.; Mootz, D. *J. Am. Chem. Soc.* **1986**, *108*, 6634. (b) Gennick, I.; Harmon, K. M. *J. Mol. Struct.* **1977**, *38*, 97.
(13) For example: (a) Cernak, J.; Orendac, M.; Potocnak, I.; Chomic, J.; Orendacova, A.; Skorsepa, J.; Feher, A. *Coord. Chem. Rev.* **2002**, *224*, 51. (b) Larionova, J.; Clérac, R.; Sanchiz, J.; Kahn, O.; Gohlen, S.; Ouahab, L. *J. Am. Chem. Soc.* **1998**, *120*, 13088. (c) Holmes, S. M.; Girolami, G. *J. Am. Chem. Soc.* **1999**, *121*, 5593. (d) Hatlevik, O.; Buschman, W. E.; Zhang, J.; Manson, J. L.; Miller, J. S. *Adv. Mater.* **1999**, *11*, 914. (e) Ferlay, S.; Mallah, T.; Ouahes, R.; Veillet, P.; Verdaguer, M. *Nature* **1995**, *378*, 701.
(14) For example: (a) Ribas, J.; Escuer, A.; Monfort, M.; Vicente, R.; Cortes, R.; Lezama, L.; Rojo, T. *Coord. Chem. Rev.* **1999**, *193*−*195*, 1027. (b) Doi, Y.; Ishida, T.; Nogami, T. *Bull. Chem. Soc. Jpn.* **2002**, *75*, 2455.
(15) For example: (a) Nardelli, M.; Gasparri, G. F.; Musatti, A.; Manfredotti, A. *Acta Crystallogr.* **1966**, *21*, 910. (b) Zurowska, B.; Mrozinski, J.; Julve, M.; Lloret, F.; Maslejova, A.; Sawka-Dobrowolska, W. *Inorg. Chem.* **2002**, *41*, 1771. (c) Vujovic, D.; Raubenheimer, H. G.; Nasimbeni, L. R. *Dalton Trans.* **2003**, 631.
(16) For example: (a) Parker, O. J.; Wolther, M. P.; Breneman, G. L. *Acta. Crystallogr., Sect. C* **1996**, *52*, 1089. (b) Grove, H.; Julve, M.; Lloret, F.; Kruger, P. E.; Tornroos, K. W.; Sletten, J. *Inorg. Chim. Acta* **2001**, *325*, 115. (c) Julve, M.; Verdaguer, M.; De Munno, G.; Real, J. A.; Bruno, G. *Inorg. Chem.* **1993**, *32*, 795.

results obtained by magnetic susceptibility, magnetization, heat capacity, and muon-spin relaxation with quantum Monte Carlo (QMC) simulations and first-principles density functional theory (DFT) calculations to determine the relevant exchange paths and exchange coupling parameters. It was also found that **1b** displays an unusual two-step saturation and $d_{x^2-y^2}$ orbital ordering; the latter trait is common to materials such as colossal magneto-resistive manganites,[17] perovskite-like $KCuF_3$,[18] and 2D K_2CuF_4,[19] which, to the best of our knowledge, rarely occurs in organic-based solids. Due to improper orientation of the Cu magnetic $d_{x^2-y^2}$ orbitals and intervening layers of Ag^+ ($S = 0$) cations, $[CuAg(H_3F_4)(pyz)_5](SbF_6)_2$ (**2**) was found to be paramagnetic for $T > 2$ K; however, unusual hysteresis in the *B*-dependent magnetization was observed. The differing hydrogen bond schemes found in **1a**, **1b**, and **2** influence the orientation of the interacting magnetic orbitals, thus causing variation in spin dimensionality.

2. Experimental Methods

Synthesis. All chemical reagents were of analytical grade and used as received. The syntheses of **1a**, **1b**, and **2** were carried out in plasticware in order to avoid fluoride abstraction of silicon from glass. $[Cu(HF_2)(pyz)_2]SbF_6$ (**1a**) was prepared by dissolving $CuF_2 \cdot yH_2O$ (~1.48 mmol, 150 mg) in 10 mL of HF(aq) (48% by wt) and adding it to a 10-mL aqueous solution containing pyrazine (236.6 mg, 2.95 mmol), NH_4HF_2 (84.3 mg, 1.48 mmol), and $NaSbF_6$ (2.95 mmol, 764.4 mg), which yielded a pale blue solution. Upon standing at room temperature overnight, the solution produced X-ray-quality deep blue plates. The sample was isolated by vacuum filtration and dried *in vacuo* (531.1 mg, 72% yield). $[Cu_2F(HF)(HF_2)(pyz)_4](SbF_6)_2$ (**1b**) was synthesized by adding the following reagents to a PTFE sample cup of a 46-mL Parr acid digestion bomb: $CuF_2 \cdot yH_2O$ (~8 mmol, 812 mg), $NaSbF_6$ (16 mmol, 4140 mg), pyrazine (16 mmol, 1280 mg), NH_4HF_2 (8 mmol, 456 mg), and 40 mL of water. The hydrothermal reaction vessel was sealed and heated at 120 °C for 3 days, after which it was removed from the oven to cool. After 24 h, the vessel was opened, and the products were collected by filtration. Blocks of compound **1b**, which are dark green-gray in color, were mechanically separated from orange crystals of $Cu(pyz)_2(SbF_6)$.[20] Compound **1b** was obtained in ~10% yield. $[CuAg(H_3F_4)(pyz)_5](SbF_6)_2$ (**2**) was prepared in the following manner: $CuCl_2 \cdot 2H_2O$ (4 mmol, 682 mg) was dissolved in 10 mL of water. In a separate beaker, $AgSbF_6$ (8.73 mmol, 3000 mg) was dissolved in 10 mL of water. The two solutions were combined and stirred, and the silver chloride that was produced was filtered off. The remaining solution was mixed with a 10-mL aqueous solution of NH_4F (6.15 mmol, 228 mg) and placed in a desiccator that contained an uncovered beaker of neat pyrazine. The pyrazine was allowed to diffuse into the solution, and after ~10 days, yellow-green, cube-like crystals were produced (18% yield) which were isolated by suction filtration. Results of elemental analysis for **1a**, **1b**, and **2** are provided in ref 21.

Caution: Hydrofluoric acid is highly corrosive and toxic and should be handled with great care.

X-ray Crystallography. The crystal structures of **1a** and **1b** were determined at 295, 150, and 90 K by use of a Siemens SMART single-crystal X-ray diffractometer equipped with a CCD-based area detector and a sealed-tube Mo Kα X-ray source with a graphite monochromator. Similar data for **2** were obtained only at 150 K. The detector frames were integrated by use of the program SAINTPlus[22] and the intensities corrected for absorption by Gaussian integration based on the measured crystal shape using the program XPREP. Other systematic variations were corrected by the analysis of replicate reflections using the program SADABS.[23] The structures were solved by use of direct methods, while full-matrix least-squares refinement on F^2 (including all data) were performed using the program package SHELXTL.[24] The program PLATON[25,26] was used to search for higher symmetry, but none was found. Non-hydrogen atoms were refined anisotropically. All H-atoms were located in difference Fourier maps at intermediate stages of refinement; however, H2 of the coordinated HF in **1b** was placed in a fixed position during final refinement. Bifluoride and $H_3F_4^-$ H-atom coordinates were refined freely with an isotropic displacement parameter $U(H)_{eq} = 1.2U_{eq}$ of the parent F-atom. For **1a** and **1b**, respectively, significant electron density was found at or near the F···F midpoint, which was consistent with the least-squares result. Pyrazine H's were placed at calculated positions and refined as riding using default values from SHELXTL.[24] Structural and refinement parameters for **1a**, **1b**, and **2**, as well as selected bond lengths and bond angles, can be found in Tables 1−6, respectively.

Infrared Spectroscopy. FTIR spectra were collected on polycrystalline samples of **1a**, **1b**, and **2** using a Pike MIRacle ATR (germanium crystal) attached to a Bruker Vertex 70 IR spectrometer running OPUS software version 5.0. Each spectrum was collected using 24 scans with a course resolution of 4 cm^{-1}.

Thermogravimetric Analysis (TGA). Data were collected on a Perkin-Elmer TGA-7 thermogravimetric analyzer in flowing nitrogen at a heating rate of 10 °C/min to a final temperature of 450 °C.

Temperature-Dependent Magnetization. Direct current measurements were conducted on a Quantum Design MPMS-7XL SQUID magnetometer equipped with the RSO option. Polycrystalline samples of **1a**, **1b**, and **2** were loaded into gelatin capsules and mounted on a carbon fiber rod. The samples were cooled in zero-field to a base temperature of 2 K and data collected on warming in a 0.1-T magnetic field. All data were corrected for temperature-independent paramagnetism and core diamagnetism using Pascal's constants.

Pulsed-Field Magnetization. Polycrystalline samples of **1a**, **1b**, and **2** were loaded into conical-shaped ampules and affixed to the end of a probe. The probe was placed in a ^{3}He cryostat where $T \geq 0.45$ K could be achieved. The sample could be inserted into and extracted from a compensated coil, *in situ*, enabling measurement of the sample's *M*. The magnet pulse width for **1a** and **1b** was ~100 ms, and measurements were made using a 65-T pulsed magnet at the National High Magnetic Field Laboratory, Los Alamos, NM. Similar experiments conducted

(17) For a recent review, see: Gor'kov, L. V.; Kresin, V. Z. *Phys. Rep.* **2004**, *400*, 149.
(18) (a) Medvedeva, J. E.; Korotin, M. A.; Anisimov, V. I.; Freeman, A. J. *Phys. Rev. B* **2002**, *65*, 172413. (b) Whangbo, M.-H.; Koo, H.-J. *Solid State Sci.* **2002**, *4*, 335.
(19) (a) Knox, K. *J. Chem. Phys.* **1959**, *30*, 991. (b) Haegele, R.; Babel, D. *Z. Anorg. Allg. Chem.* **1974**, *409*, 11.
(20) Crystallographic data for $Cu(pyz)_2(SbF_6)$: monoclinic space group $P2_1/c$, with $a = 7.9725(8)$, $b = 8.4866(9)$, and $c = 10.8938(11)$ Å, $\alpha = 89.841(3)$, $\beta = 84.921(2)$, and $\gamma = 63.859(2)°$, $V = 658.54(12)$ Å^3, $T = 298$ K, $Z = 2$, $\mu = 3.731$ mm^{-1}, $R_1(F_o) = 0.0245$ ($I > 2\sigma$; 2440 reflections), $R_w(F_o^2) = 0.0580$ (all data; 2590 reflections). The structure consists of a 1D zigzag chain formed by the linking of tetrahedral CuN_3F units via bridging pyz ligands. An ORTEP diagram, along with atom labeling scheme, and crystal packing diagram are provided as Supporting Information.
(21) Elemental analyses: (**1a**) Anal. Calcd (%) for $C_8H_9N_4F_8SbCu$: C, 19.28; H, 1.82; N, 11.24. Found: C, 19.62; H, 2.13; N, 11.31. (**1b**) Anal. Calcd (%) for $C_{16}H_{18}N_8F_{16}Sb_2Cu_2$: C, 19.28; H, 1.82; N, 11.24. Found: C, 19.41; H, 2.07; N, 11.26. (**2**) Anal. Calcd (%) for $C_{20}H_{23}N_{10}F_{16}Sb_2CuAg$: C, 21.39; H, 2.07; N, 12.48. Found: C, 21.51; H, 2.40; N, 12.54.
(22) *SAINTPlus*, v. 7.23a, Data Reduction and Correction Program; Bruker AXS: Madison, WI, 2004.
(23) *SADABS*, v. 2004 1, an empirical absorption program; Bruker AXS Inc.: Madison, WI, 2004.
(24) Sheldrick, G. M. *SHELXTL*, v. 6.14, Structure Determination Software Suite; Bruker AXS Inc.: Madison, WI, 2004.
(25) Spek, A. L. Utrecht University, Utrecht, The Netherlands, 1999.
(26) Spek, A. L. *J. Appl. Crystallogr.* **2003**, *36*, 7–13.

Table 1. X-ray Crystallographic Refinement Details for $[Cu(HF_2)(pyz)_2]SbF_6$ (**1a**)

	T (K)		
	90(2)	150(2)	295(2)
formula		$C_8H_9N_4F_8SbCu$	
formula weight (g/mol)		498.48	
crystal size, mm	0.15 × 0.14 × 0.01	0.56 × 0.44 × 0.28	0.15 × 0.14 × 0.01
space group	*P4/nmm*	*P4/nmm*	*P4/nmm*
a, Å	9.7044(2)	9.719(2)	9.7200(6)
b, Å	9.7044(2)	9.719(2)	9.7200(6)
c, Å	6.8538(3)	6.865(3)	6.9414(9)
β, °	90	90	90
V, Å^3	645.46(3)	648.5(4)	655.8(1)
Z	2	2	2
ρ_{calc}, g/cm^3	2.565	2.553	2.524
λ, Å	0.71073	0.71073	0.71073
μ, mm^{-1}	3.839	3.821	3.778
$R(F)^a$	0.0144	0.0175	0.0182
$R_w(F)^b$	0.0359	0.0452	0.0489
GOF	1.090	1.103	1.083

^{a} $R = \sum[|F_o| - |F_c|]/\sum|F_o|$. ^{b} $R_w = [\sum w[|F_o| - |F_c|]^2/\sum w[|F_o|^2]^{1/2}$.

Table 2. X-ray Crystallographic Refinement Details for $[Cu_2F(HF)(HF_2)(pyz)_4](SbF_6)_2$ (**1b**)

	T (K)		
	90(2)	150(2)	295(2)
formula		$C_{16}H_{18}N_8F_{16}Sb_2Cu_2$	
formula weight (g/mol)		996.96	
crystal size, mm	0.22 × 0.20 × 0.04	0.60 × 0.48 × 0.44	0.22 × 0.20 × 0.04
space group	*Cmca*	*Cmca*	*Cmca*
a, Å	13.5926(5)	13.589(2)	13.688(2)
b, Å	19.9573(7)	19.974(3)	20.055(3)
c, Å	19.8663(7)	19.893(3)	19.976(3)
β, °	90	90	90
V, Å^3	5389.2(3)	5399.6(11)	5483.5(14)
Z	8	8	8
ρ_{calc}, g/cm^3	2.458	2.453	2.415
λ, Å	0.71073	0.71073	0.71073
μ, mm^{-1}	3.678	3.671	3.615
$R(F)^a$	0.0218	0.0233	0.0283
$R_w(F)^b$	0.0537	0.0710	0.0636
GOF	1.087	1.079	1.148

^{a} $R = \sum[|F_o| - |F_c|]/\sum|F_o|$. ^{b} $R_w = [\sum w[|F_o| - |F_c|]^2/\sum w[|F_o|^2]^{1/2}$.

Table 3. X-ray Crystallographic Refinement Details for $[CuAg(H_3F_4)(pyz)_5](SbF_6)_2$ (**2**) at 150(2) K

formula	$C_{20}H_{23}N_{10}F_{16}Sb_2CuAg$
formula weight (g/mol)	1122.39
crystal size, mm	0.28 × 0.20 × 0.08
space group	*Cmma*
a, Å	15.0944(6)
b, Å	15.5893(7)
c, Å	14.7562(6)
β, °	90
V, Å^3	3472.3(3)
Z	4
ρ_{calc}, g/cm^3	2.370
λ, Å	0.71073
μ, mm^{-1}	2.816
$R(F)^a$	0.0390
$R_w(F)^b$	0.0994
GOF	1.304

^{a} $R = \sum[|F_o| - |F_c|]/\sum|F_o|$. ^{b} $R_w = [\sum w[|F_o| - |F_c|]^2/\sum w[|F_o|^2]^{1/2}$.

Table 4. Selected Bond Lengths (Å) and Bond Angles (°) for $[Cu(HF_2)(pyz)_2]SbF_6$ (**1a**)

	T (K)		
	90(2)	150(2)	295(2)
Cu1−N1	2.041(2)	2.044(2)	2.049(3)
Cu1−F1	2.284(2)	2.289(2)	2.338(3)
H1−F1	1.143(2)	1.143(2)	1.133(3)
F1···F1A	2.286(2)	2.286(2)	2.266(6)
Sb1−F2	1.875(3)	1.872(4)	1.873(6)
Sb1−F3	1.872(3)	1.863(4)	1.843(6)
Sb1−F4	1.882(2)	1.882(2)	1.869(3)
N1−C1	1.341(2)	1.342(2)	1.331(3)
N1−Cu1−N1A	90	90	90
N1−Cu1−F1	90	90	90
F1−Cu1−F1A	180	180	180
Cu1−F1−H1	180	180	180
Cu1−N1−C1	121.5(1)	121.5(1)	121.6(1)
F1···H1···F1A	180	180	180
F2−Sb1−F3	180	180	180
F2−Sb1−F4	89.48(5)	89.09(5)	89.0(1)

on **2** were made using a 50-T pulsed magnet (∼10 ms pulse width) at the Nicholas Kurti Magnetic Field Laboratory, Oxford University, UK.

Heat Capacity. The heat capacity values of **1a** and **1b** were measured in zero-field using a Quantum Design Physical Properties Measurement System (PPMS) between 0.4 and 200 K, using a standard relaxation time technique. Separate runs were taken for 0.4−40 K and 2−200 K and the results combined. Contributions from the Apiezon-N grease and the sample holder were subtracted automatically. Absolute values of the heat capacity should be accurate to within ∼5%, primarily limited by the precision of the calorimeter.

Table 5. Selected Bond Lengths (Å) and Bond Angles (°) for $[Cu_2F(HF)(HF_2)(pyz)_4](SbF_6)_2$ (**1b**)

	T (K)		
	90(2)	150(2)	295(2)
Cu1−N1	2.091(2)	2.094(2)	2.130(3)
Cu1−N12A	2.393(2)	2.405(2)	2.413(3)
Cu1−F1	1.908(3)	1.907(3)	1.911(4)
Cu2−N2	2.024(2)	2.023(2)	2.029(3)
Cu2−N11	2.012(2)	2.018(2)	2.024(3)
Cu2−F3	2.257(2)	2.257(2)	2.283(2)
H3−F3	1.159(8)	1.142(3)	1.142(6)
F3···F3A	2.283(3)	2.281(4)	2.277(5)
H2−F2	0.951	0.953	0.962
C1−N1	1.343(4)	1.347(4)	1.338(5)
C2−N2	1.345(4)	1.347(4)	1.347(5)
Sb1−F21	1.880(2)	1.871(2)	1.873(3)
Sb1−F22	1.919(3)	1.915(4)	1.909(4)
Sb1-*F*23	1.887(2)	1.881(3)	1.875(4)
Sb1−F24	1.886(3)	1.881(3)	1.874(4)
Sb1−F25	1.895(3)	1.899(3)	1.890(4)
Sb2−F11	1.913(3)	1.916(4)	1.918(5)
Sb2−F12	1.891(3)	1.884(3)	1.874(4)
Sb2−F13	1.879(2)	1.874(2)	1.874(3)
Sb2−F14	1.887(3)	1.890(3)	1.876(4)
Sb2−F15	1.895(3)	1.900(3)	1.899(4)
N1−Cu1−N1A	180.0(1)	179.7(1)	179.8(2)
N1−Cu1−F1	89.98(7)	90.13(7)	90.1(1)
F1−Cu1−F2	180	180	180
F1−Cu1−N12A	89.90(7)	90.14(6)	90.14(9)
Cu1−F2−H2	120.9	121.0	121.5
F3···H3···F3A	160(5)	174(5)	171(7)
N11−Cu2−N11A	88.9(1)	88.9(1)	88.7(2)
N11−Cu2−N2	178.94(9)	178.6(1)	178.7(1)
N2−Cu2−N2A	91.0(1)	91.3(1)	91.2(2)
N11−Cu2−F3	90.35(9)	89.96(9)	90.0(1)
Cu2−F3−H3	170(2)	177(2)	175(4)
F21−Sb1−F21	178.8(1)	179.0(1)	178.6(2)
F21−Sb1−F23	90.24(5)	90.25(6)	90.2(1)
F22−Sb1−F24	92.5(1)	92.9(1)	92.9(2)
F22−Sb1−F25	179.9(1)	180.0(1)	179.9(2)
F11−Sb2−F13	90.39(6)	90.35(7)	90.53(9)
F12−Sb2−F13	89.76(6)	89.77(6)	89.8(1)
F12−Sb2−F14	175.0(1)	174.7(2)	174.5(2)
F13−Sb2−F13	179.1(1)	179.2(1)	178.9(2)
F14−Sb2−F15	86.9(1)	86.9(1)	86.9(2)

Table 6. Selected Bond Lengths (Å) and Bond Angles (°) for $[CuAg(H_3F_4)(pyz)_5](SbF_6)_2$ (**2**) at 150 K

Cu1−N10	2.035(5)	Sb1−F1	1.884(5)
Cu1−N20	2.374(7)	Sb1−F2	1.908(6)
Cu1−F10	2.015(5)	Sb1−F3	1.887(3)
Ag1−N11	2.556(6)	C10−N10	1.333(5)
Ag1−N30	2.390(5)	C20−N20	1.336(6)
Ag1−N40	2.501(6)	C30−N30	1.327(5)
F10···H10	1.33(7)	H10···F11	1.34(7)
F10−Cu1−F10A	180	F10···H10···F11	167(3)
N10−Cu1−F10	90	F1−Sb1−F2	180
N10−Cu1−N20	90	F1−Sb1−F3	88.99(8)
N11−Ag1−N11A	180	F3−Sb1−F3A	178.0(2)
N30−Ag1−N30A	180	Cu1−N10−C10	121.7(3)
N30−Ag1−N40	90	Cu1−F10−H10	141(3)

Muon-Spin Relaxation (μSR). Zero-field measurements[27] were made on **1a** at the ISIS Pulsed Muon Facility, Rutherford Appleton Laboratory, UK, using the MuSR spectrometer. Measurements performed on **1b** were carried out at the Swiss Muon Source, Paul Scherrer Institute, Switzerland, using the LTF instrument. Polycrystalline samples of each were packed in a 12.5-μm Ag foil pouch and mounted on a Ag plate inside a ^{3}He sorption cryostat (**1a**) or dilution refrigerator (**1b**).

Quantum Monte Carlo Simulations. The stochastic series expansion (SSE) method[28,29] is a finite-temperature QMC technique based on importance sampling of the diagonal matrix elements of the density matrix $e^{-\beta H}$. Using the "operator-loop" cluster update,[29] the autocorrelation time for the system sizes we considered here (up to $\sim 3 \times 10^4$ spins) was at most a few Monte Carlo sweeps, even at the critical temperature.[30] Estimates of ground-state observables were obtained by using sufficiently large values of the inverse temperature, β. We used parallel tempering,[31,32] where several simulations were run simultaneously on a parallel computer, using a fixed value of $J_\perp$ and different, but closely spaced, values of h over the entire range of fields up to saturation. Along with the usual Monte Carlo updates, we swapped the values of fields for SSE configurations (processes) with adjacent values of h at regular intervals (typically after every Monte Carlo step, each time attempting several hundred swaps).

Electronic Structure Calculations. To evaluate the spin exchange parameters of possible pathways in **1a** and **1b**, first-principles density functional theory (DFT) spin-polarized electronic structure calculations were carried out for the high-spin (HS) and broken-symmetry (BS) states of the spin dimers associated with the spin exchange paths (i.e., structural units consisting of two adjacent Cu^{2+} ion sites). Our calculations were carried out by employing the B3LYP exchange-correlation functional[33,34] and the 6-31G* basis set encoded in the Gaussian 03 B.04 program package.[35] The electronic energies of the HS and BS states of a spin dimer are defined as E_{HS} and E_{BS}, respectively. Since each spin site is a spin-1/2 Cu^{2+} ion, the exchange parameter J associated with a spin dimer is related to E_{HS} and E_{BS} by $J = E_{BS} - E_{HS}$.[36,37] We use the convention in which the strength of a spin exchange interaction is expressed as J instead of $2J$.

3. Crystal Structures

3.1. $[Cu(HF_2)(pyz)_2]SbF_6$ (1a). The crystal structure of **1a** is analogous to $[Cu(HF_2)(pyz)_2]BF_4$, with octahedral SbF_6^- anions replacing interstitial BF_4^- ions.[10] An ORTEP diagram along with the atom labeling scheme is shown in Figure 1 for the 295 K structure. The Cu^{2+} ion occupies a $\bar{4}2m$ site and exhibits a classical 4+2 Jahn−Teller elongated stereochemistry consisting of four equatorial pyrazine N-atoms [Cu1−N1 = 2.049(3) Å], while the longer axial sites are occupied by F-atoms [Cu1−F1 = 2.338(3) Å] from two different HF_2^- ions. Owing to the high symmetry of the Cu site, the F1−Cu1−N1, N1−Cu1−N1A, and F1−Cu1−F1A bond angles are ideal, i.e., 90° and 180°. The HF_2^- anion features symmetric H···F bonds of 1.133(3) Å and a F···F distance of 2.266(6) Å, the latter being ~0.06 Å longer than that found in $[Cu(HF_2)(pyz)_2]BF_4$.[10] The H1−F1−Cu1 bond angle is 180°, and C1−N1−Cu1 is 121.6(1)°. The intramolecular C−C and C−N bond distances as well as C−C−N and C−N−C bond angles of the pyrazine

(27) Blundell, S. J. *Contemp. Phys.* **1999**, *40*, 175.
(28) (a) Sandvik, A. W.; Kurkijarvi, J. *Phys. Rev. B* **1991**, *43*, 5950. (b) Sandvik, A. W. *Phys. Rev. B* **1997**, *56*, 11678.
(29) Sandvik, A. W. *Phys. Rev. B* **1999**, *59*, R14157.
(30) Syljuasen, O. F.; Sandvik, A. W. *Phys. Rev. E* **2002**, *66*, 046701.
(31) Marinari, E. *Advances in computer simulation*, Lecture Notes in Physics, Vol. 501, lectures held at the Eötvös Summer School in Budapest, Hungary, 16−20 July 1996; Kertsz, J., Kondor, I., Eds.; Springer: Berlin, 1998.
(32) (a) Hukushima, K.; Takayama, H.; Nemoto, K. *Int. J. Mod. Phys. C* **1996**, *7*, 337. (b) Hukushima, K.; Nemoto, K. *J. Phys. Soc. Jpn.* **1996**, *65*, 1604.
(33) Becke, D. *Phys. Rev. A* **1988**, *38*, 3098.
(34) Lee, C.; Yang, W.; Parr, R. G. *Phys. Rev. B* **1988**, *37*, 785.
(35) Frisch, M. J.; et al. *Gaussian 03*, version B.04; Gaussian, Inc.: Pittsburgh, PA, 2003.
(36) (a) Dai, D.; Whangbo, M.-H. *J. Chem. Phys.* **2001**, *114*, 2887. (b) Noodleman, L. *J. Chem. Phys.* **1981**, *74*, 5737.
(37) Whangbo, M.-H.; Koo, H.-K.; Dai, D. *J. Solid State Chem.* **2003**, *176*, 417.

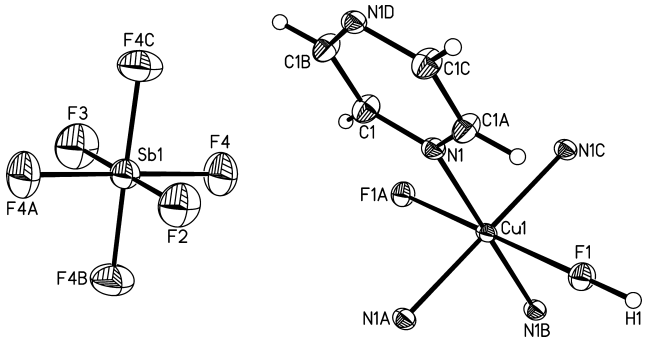

Figure 1. ORTEP drawing of the asymmetric unit and atom labeling scheme for **1a** at 295 K. Thermal ellipsoids are drawn at the 35% probability level.

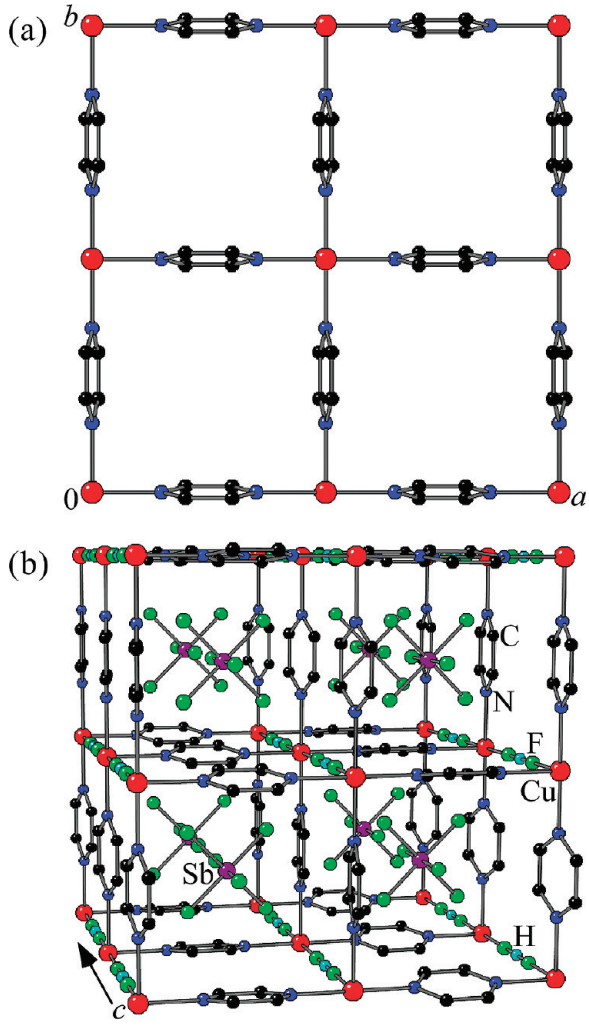

Figure 2. (a) Portion of a 2D $[Cu(pyz)_2]^{2+}$ sheet for **1a** viewed along the *c*-axis. (b) 3D framework of **1a** comprised of 2D sheets connected by the Cu−F···H···F−Cu linkages along the *c*-direction. Pyrazine H-atoms are not shown for clarity. Both figures correspond to the 295 K structure.

ligand are in agreement with those found in other compounds as well as **1b** and **2**.[10,38,39a,b]

The extended structure of **1a** is polymeric and consists of 2D $[Cu(pyz)_2]^{2+}$ sheets confined to the *ab*-plane (Figure 2a), while the axial positions are occupied by linearly bridging $\mu_{1,3}$-HF_2^- ions along the *c*-axis, thus forming a 3D network (Figure 2b). By comparison, $Cu(ClO_4)_2(pyz)_2$ has a similar 2D architecture; however, the ClO_4^- anions do not bridge the 2D $[Cu(pyz)_2]^{2+}$ sheets.[39] The ClO_4^- anions pack between the layers in a manner that forces the sheets to be mutually staggered and relatively far apart. From Figure 2, it can be seen that the pyrazine ligands in **1a** counter-rotate in a pattern consistent with the four-fold symmetry of each Cu^{2+} site as in $[Cu(HF_2)(pyz)_2]BF_4$; however, the ring tilt angle (relative to the CuN_4 plane) is much larger at 81.4(1)° and nearly parallel to the *c*-axis, as compared to the angle of 59.4(2)° found in the BF_4^- analogue. Corresponding pyz tilt angles of 61.4° and 59.7° have been reported for structurally related $[Cu(NO_3)(pyz)_2]PF_6$[39a] and $[Cu(NO_2)(pyz)_2]ClO_4$.[40]

The framework of **1a** is pseudocubic and similar to that of α-Po, owing to the nearly equivalent Cu···Cu separations along the Cu−pyz−Cu [6.8731(6) Å] and Cu−F···H···F−Cu [6.9414(9) Å] bridges. SbF_6^- ions are displaced by 0.294 Å (along *c*) away from the ideal body-centered position. The ionic volume of SbF_6^- (71 Å^3) is nearly twice that of BF_4^- (38 Å^3),[41] and while the Cu−F···H···F−Cu separation is ∼0.1 Å longer than that found in $[Cu(HF_2)(pyz)_2]BF_4$ [i.e., 6.8519(3) Å], the H···F and Cu−F bonds increase in length in order to accommodate the bulkier SbF_6^- ion. There are long H1A···F4 contacts of 2.575 Å between the pyz ring and SbF_6^- anion. Other than the dramatic change in pyz tilt angle, the geometry of the $[Cu(pyz)_2]^{2+}$ sheets remains largely unaffected by the anion substitution.

As **1a** is cooled to 90 K, there is little change in the structure other than the usual lattice contraction, with the unit cell shrinking by only 1.6%. The less rigid Cu−F···H···F−Cu bonds are more sensitive to a temperature change, which leads to a 1.7% reduction along the *c*-direction and slightly shorter Cu−F bond distances of 2.284(2) Å. The decrease in the unit cell size and reduced thermal motion induces a slightly smaller pyz tilt angle of 79.1(1)° and a subtle shortening of intermolecular H···F hydrogen bonds to 2.532 Å.

3.2. $[Cu_2F(HF)(HF_2)(pyz)_4](SbF_6)_2$ (1b). From Figure 3 it can be seen that there are two crystallographically unique Cu^{2+} sites, labeled Cu1 and Cu2, and shown as orange and red spheres, respectively, in Figure 4. The Cu1 atom is coordinated to a fluoride ion (F1), the F atom of an HF (F2),[42] and N-donor atoms from four different pyrazine ligands. For Cu1 (at 295 K), $Cu1F_2N_2$ defines the equatorial plane, with Cu1−F1 = 1.911(4), Cu1−F2 = 1.910(4), and Cu1−N1 = 2.130(3) Å. The axial sites are occupied by two equivalent N12-donor atoms [Cu1−N12 = 2.413(3) Å]. In contrast, each Cu2 atom is coordinated to two N2- and two N11-donors to form the $Cu2N_4$ equatorial plane [Cu2−N2 = 2.029(3) and Cu2−N11 =

(38) For example: (a) Otieno, T.; Gipson, A. M.; Parkin, S. *J. Chem. Crystallogr.* **2002**, *32*, 81. (b) Heier, K. R.; Norquist, A. J.; Halasyamani, P. S.; Duarte, A.; Stern, C. L.; Poeppelmeier, K. R. *Inorg. Chem.* **1999**, *38*, 762. (c) Dong, Y.-B.; Smith, M. D.; Layland, C.; zur Loye, H.-C. *Inorg. Chem.* **1999**, *38*, 5027. (d) Kitagawa, S.; Okubo, T.; Kawata, S.; Kondo, M.; Katada, M.; Kobayashi, H. *Inorg. Chem.* **1995**, *34*, 4790. (e) Haynes, J. S.; Rettig, S. J.; Sams, J. R.; Thompson, R. C.; Trotter, J. *Can. J. Chem.* **1987**, *65*, 420.
(39) (a) Woodward, F. M.; Gibson, P. J.; Jameson, G. B.; Landee, C. P.; Turnbull, M. M.; Willett, R. D. *Inorg. Chem.* **2007**, *46*, 4256. (b) Darriet, J.; Haddad, M. S.; Duesler, E. N.; Hendrickson, D. N. *Inorg. Chem.* **1979**, *18*, 2679. (c) Lancaster, T.; Blundell, S. J.; Brooks, M. L.; Baker, P. J.; Pratt, F. L.; Manson, J. L.; Conner, M. M.; Xiao, F.; Landee, C. P.; Chaves, F. A.; Soriano, S.; Novak, M. A.; Papageorgiou, T.; Bianchi, A. D.; Herrmannsdörfer, T.; Wosnitza, J.; Schlueter, J. A. *Phys. Rev. B* **2007**, *75*, 094421.
(40) Liu, T.; Chen, Y.-H.; Zhang, Y.-J.; Wang, Z.-M.; Gao, S. *Inorg. Chem.* **2006**, *45*, 9148.
(41) Mingos, D. M. P.; Rohl, A. L. *Inorg. Chem.* **1991**, *30*, 3769.

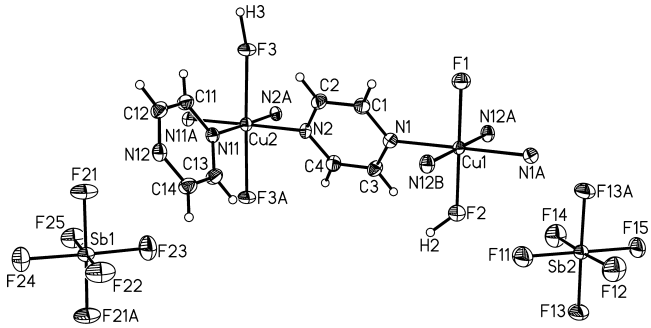

Figure 3. ORTEP diagram and atom labeling scheme for **1b** at 295 K. Thermal displacement parameters are drawn at the 35% probability level. Due to positional disorder, only one of the two possible positions for H2 is shown.

2.024(3)], with two F3 ions from $\mu_{1,3}$-HF_2^- bridges occupying the axial positions [Cu2−F3 = 2.283(2) Å].

Two-dimensional sheets that contain the $Cu1F_2N_2$ and the $Cu2N_4$ equatorial planes in **1b** lie parallel to the *bc*-plane (Figure 4a) and are connected by the HF_2^- anions along the *a*-direction (Figure 4b), which form $\mu_{1,3}$-bridges between the Cu2 atoms [Cu2···Cu2 = 6.844(2) Å]. The HF_2^- ligand has symmetric H3···F3 bond lengths of 1.142(6) Å and a nonlinear F3···H3···F3A bond angle of 171(7)°. A metal-coordinated HF [H2−F2 = 0.962 Å] is unusual but has been observed in $[pipzH_2]_4$-$[MnF_4(H_2O)_2][MnF_4(HF)_2][Mn_4F_{18}]$.[43] Cu1 and Cu2 alternate regularly within a layer; however, along the *a*-direction, like ions form segregated chains. The pyz bridges experience a smaller tilt angle of 66.8(2)° away from the CuN_4 plane, as compared to the corresponding angle observed in **1a**. Although every other HF_2^- bridge contains a broken H···F bond in **1b**, the chemical structures of **1a** and **1b** contain the same molecular components and nearly identical 3D frameworks, and perhaps unusual, we consider **1b** to be a defective polymorph of **1a**.

A close comparison of the structures of **1a** (Figure 2b) and **1b** (Figure 4b) reveals interesting differences with regard to the pyz ring orientation. In **1a**, the rings lie parallel to one another along the $[Cu(pyz)_2]^{2+}$ sheet stacking axis (i.e., *c*-axis) but counter-rotate relative to one another within a sheet. For **1b**, the rings counter-rotate along all directions such that successive rings along the $[Cu(pyz)_2]^{2+}$ sheet stacking direction (i.e., *a*-axis) point toward the same SbF_6^- anion. At 90 K, the pyz ligands remain in the same configuration for both **1a** and **1b**; however, they become slightly more tilted [68.1(2)°] in **1b**.

3.3. $[CuAg(H_3F_4)(pyz)_5](SbF_6)_2$ (2). Compound **2** is bimetallic, contains an ordered arrangement of octahedrally coordinated Cu^{2+} and Ag^+ cations (Figure 5), and contains bridging $H_3F_4^-$ ions. Because both cations occupy 222 sites, donor atoms

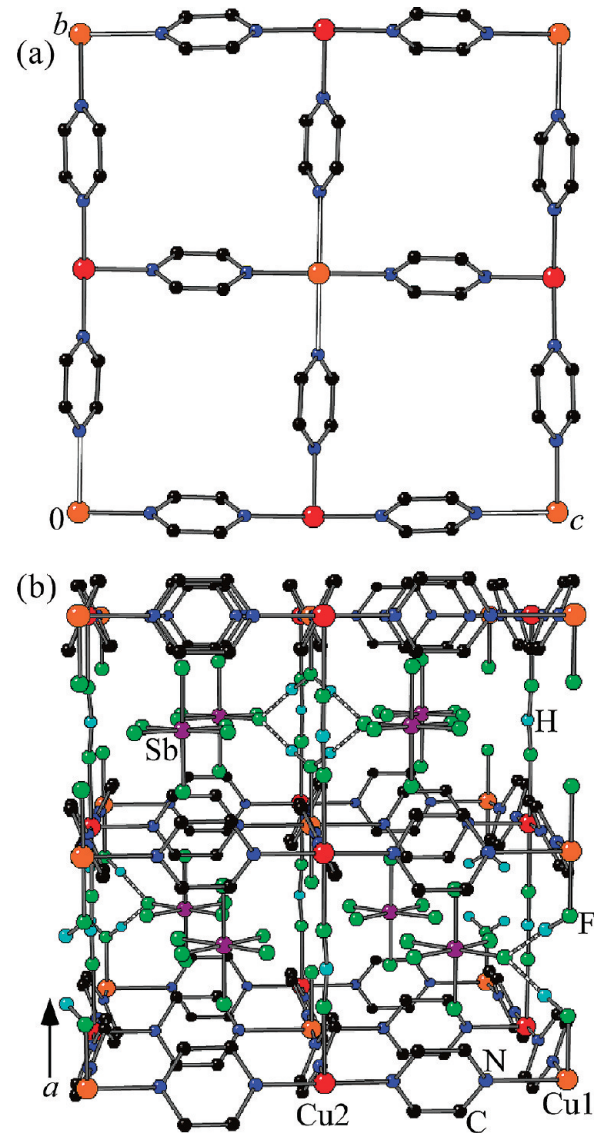

Figure 4. (a) 2D $[Cu(pyz)_2]^{2+}$ sheet of **1b** viewed normal to the *bc*-plane. Open bonds indicate longer Jahn−Teller axes. (b) Defect structure of **1b** at 295 K. Pyrazine H-atoms are omitted for clarity. Dashed lines delineate hydrogen bonds.

situated *trans* to one another are related by symmetry. Similar to 3D pseudocubic $[Ag(pyz)_3]SbF_6$,[44] the Ag^+ ion in **2** is coordinated to six different μ-pyz N-donor atoms with average Ag−N distances of 2.48(8) Å at 150 K. The coordination environment of Cu1 is Jahn−Teller elongated along the N20−Cu−N20A direction, giving Cu1−N bond lengths of 2.374(7) Å. The nonmagnetic d_{z^2} orbitals of each Cu site share a common orientation and lie along the *a*-axis but are not considered to be orbitally ordered.

The $H_3F_4^-$ ion observed in **2** is geometrically unique in that it has a rhombic-like motif and forms a bridge between Cu^{2+} ions, and because of disorder, three of the four H positions are randomly occupied. As noted previously, the $H_3F_4^-$ ion found in KH_3F_4 is known to exhibit C_{3v} symmetry, where a central fluoride ion is hydrogen-bonded to three additional HF molecules.[12] For **2** the H10···F10 and H10···F11 distances of ∼1.34 Å are significantly longer than those found for symmetric

(42) It should be noted that similar *R*, R_w, and GOF parameters were obtained if the ligand was treated as either a disordered HF or a fully occupied H_2O. More convincing evidence for the existence of a HF ligand was the more regular shape and size of the F thermal ellipsoid; attempts to model this coordinated atom as oxygen led to an abnormally small and deformed displacement parameter. We cannot rule out the possibility of a mixed HF/H_2O site. Elemental analyses to determine oxygen content would yield results that exceed expectation due to the formation of additional H_2O (and SiF_4), as the sample is pyrolized in the quartz tube to produce HF. Because HF and H_2O have very similar molecular weights, TGA is insensitive to this possibility; however, the IR data are consistent with the absence of H_2O. Whether the coordinated ligand is HF or H_2O will not affect our interpretation of the magnetic behavior.

(43) Stief, R.; Massa, W. *Z. Anorg. Allg. Chem.* **2004**, *630*, 2502.

(44) Carlucci, L.; Ciani, G.; Proserpio, D. M.; Sironi, A. *Angew. Chem., Int. Ed.* **1995**, *34*, 1895.

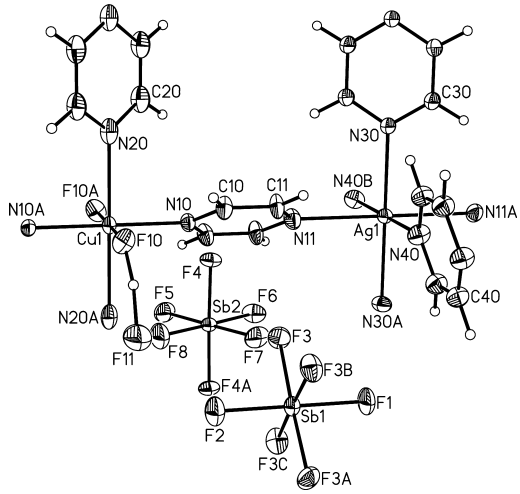

Figure 5. ORTEP diagram and atom labeling scheme for **2** at 150 K. Thermal displacement parameters are drawn at the 35% probability level. The SbF_6^- anion that contains Sb2 is positionally disordered between two sites; thus, only the site of highest occupancy is shown for clarity.

HF_2^- but comparable to those reported in KH_3F_4[12] and $[Cu(dpd)_2](H_2F_3)_2$.[11a] The fact that we observe a different structure is not unexpected owing to the differences in the chemical species present as well as crystal packing.

The structure of **2** is similar to those of **1a** and **1b** in that it consists of a 3D network where pyz ligands link the metal ions into nominally 2D square sheets, as shown in Figure 6a. Alternating $[Cu(pyz)(H_3F_4)]^+$ and $[Ag(pyz)_2]^+$ layers lie parallel to the *ab*-plane. These sheets are linked through pyz ligands along the *c*-direction to yield the 3D network illustrated in Figure 6b. Intralayer Cu···Cu and Cu···Ag distances are 7.5472(6) (along *a*) and 7.3781(6) Å (along *c*), respectively, whereas the interlayer Cu···Cu and Ag···Ag separations along the *b*-direction are equidistant at 7.7947(7) Å. The pyz ligands also tilt, but depending on the metal ion to which they are attached, two distinct Cu−pyz tilt angles [54.1(2)° and 28.6(2)° away from the *ab*- and *bc*-planes, respectively] and two unique Ag−pyz tilt angles [61.5(2)° and 12.1(2)° out of the *bc*- and *ab*-planes] are observed.

4. Thermogravimetric Analyses

The thermogravimetric analyses of $[Cu(HF_2)(pyz)_2]SbF_6$ (**1a**) and $[Cu_2F(HF)(HF_2)(pyz)_4](SbF_6)_2$ (**1b**) indicate that they are thermally stable to ∼250 and 215 °C, respectively, while **2** undergoes an initial weight loss of ∼4% (likely the liberation of HF) between 80 and 115 °C (Figure 7). Because the copper pyrazine sheets, hexafluoroantimonate anions, and HF adducts are common to all three structures, the difference in the onset of decomposition is most likely due to the difference in bonding nature of the HF molecule that exists in each. The initial weight loss of ∼9% in **1b** is due to loss of HF/F of the broken bifluoride (theory 8%), whereas the gradual ∼30% weight loss up to about 300 °C is attributed to evolution of pyrazine (theory 32%). This is similar to $CuF_2(H_2O)_2(pyz)$,[45] where the bridging pyrazine is also lost in the 200−300 °C range. In **2**, two bridging pyz ligands are lost between 115 and 205 °C, while the remaining

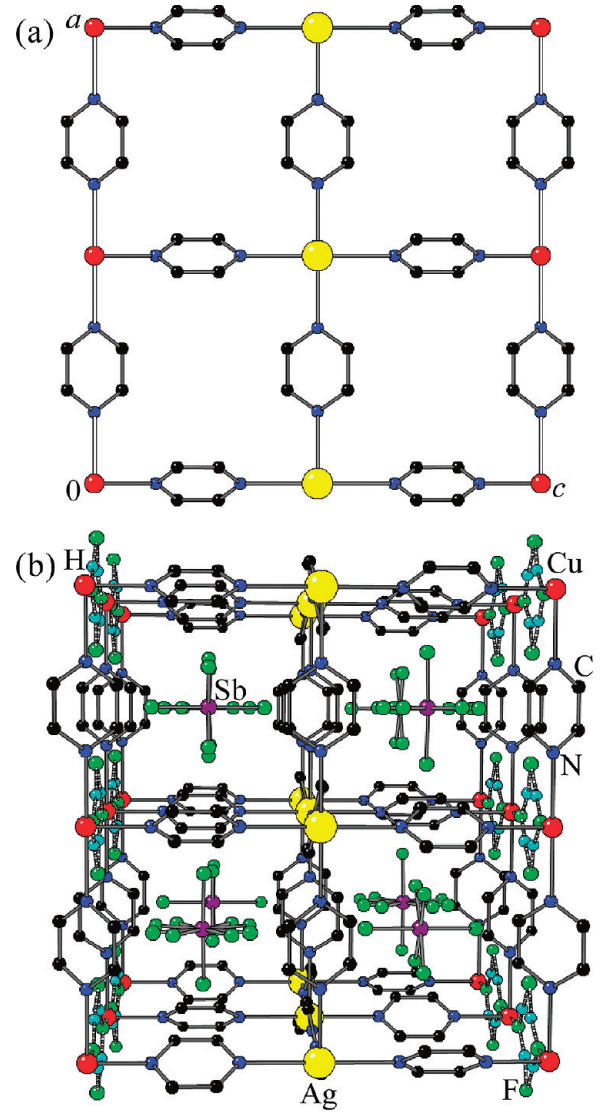

Figure 6. (a) 2D $[CuAg(pyz)_2]^{3+}$ sheet of **2** viewed down the *b*-direction. Open bonds delineate Jahn−Teller axes. (b) 3D network of **2** showing the alternation of 2D $[Cu(pyz)(H_3F_4)]^+$ and $[Ag(pyz)_2]^+$ sheets. Pyrazine H-atoms have been omitted for clarity. Dashed lines indicate hydrogen bonds.

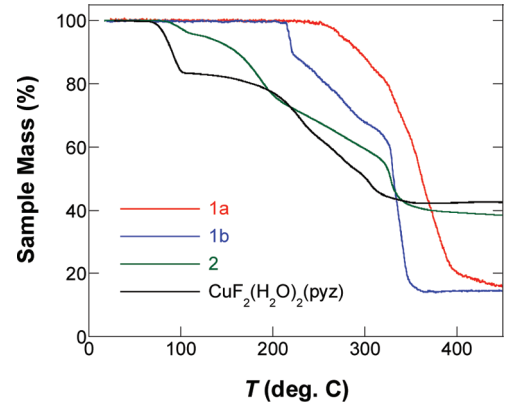

Figure 7. TGA data for $[Cu(HF_2)(pyz)_2]SbF_6$ (**1a**), $[Cu_2F(HF)(HF_2)(pyz)_4](SbF_6)_2$ (**1b**), $[CuAg(H_3F_4)\text{-}(pyz)_5](SbF_6)_2$ (**2**), and chemically related $CuF_2(H_2O)_2(pyz)$.

pyz ligands dissociate between 205 and 350 °C. For temperatures greater than 325 °C, **1a**, **1b**, and **2** exhibit rapid weight

(45) Manson, J. L.; Conner, M. M.; Schlueter, J. A.; McConnell, A. C.; Southerland, H. I.; Malfant, I.; Lancaster, T.; Blundell, S. J.; Brooks, M. L.; Pratt, F. L.; Singleton, J.; McDonald, R. D.; Lee, C.; Whangbo, M.-H. *Chem. Mater.* **2008**, *20*, 7408.

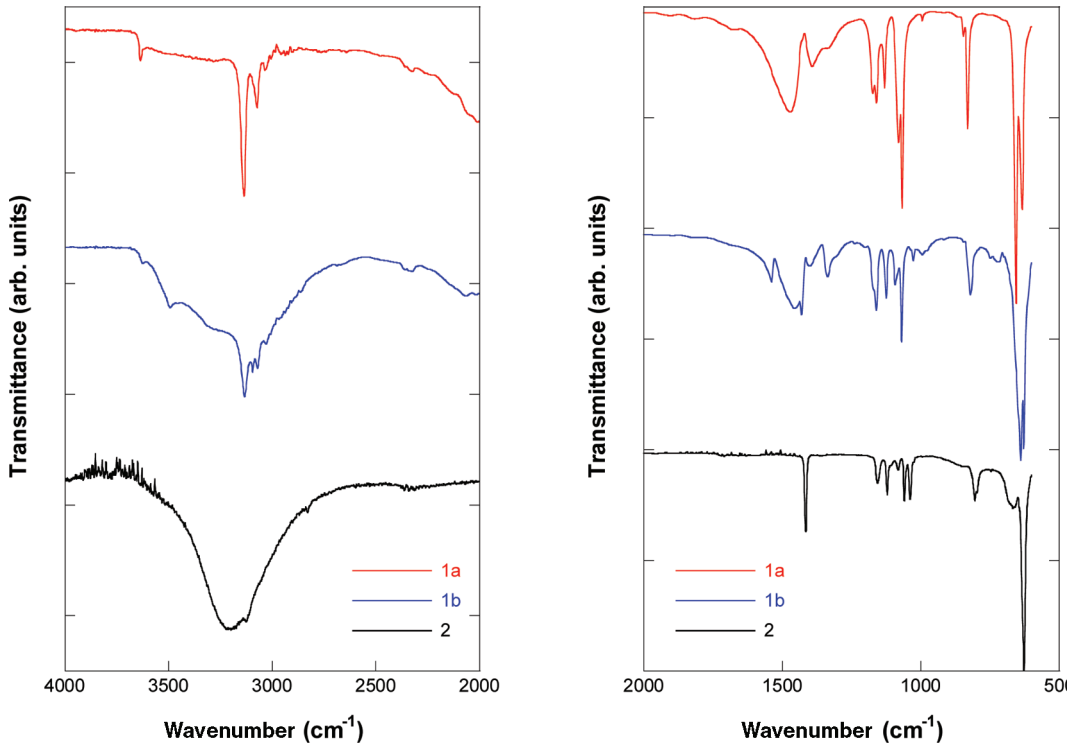

Figure 8. Room temperature mid-IR spectra for compounds **1a**, **1b**, and **2**.

Table 7. Room Temperature Mid-IR Absorption Data (Resolution = ±4 cm^{-1})[a] for $[Cu(HF_2)(pyz)_2]SbF_6$ (**1a**), $[Cu_2F(HF)(HF_2)(pyz)_4](SbF_6)_2$ (**1b**), and $[CuAg(H_3F_4)(pyz)_5](SbF_6)_2$ (**2**)

mode	1a	1b	2
pyz; C−H stretch	3137w, 3074w	3133w, 3094w, 3072w	3122w (sh)
pyz; ring stretch + bend	obscured	1430m	1415m
pyz; ring bend	1172m, 1160m, 1132m, 1081m, 1067s	1169m (sh), 1161m, 1125m, 1092m, 1069m	1156m, 1121m, 1108w, 1082m, 1059m, 1038m
pyz; C−H bend	847w, 831s	830w (sh), 821m	804m, 797w
Sb−F stretch + out-of-plane bend	657s, 636s	656m (sh), 648s (sh), 640s, 627s	634s (sh), 627s
H···F stretch	2860−3670w (br)	2580−3670w (br)	2580−3700w (br)
H···F bend	1473m	1539m (HF), 1456m (HF_2^-)	absent

[a] s = strong, m = medium, w = weak, sh = shoulder, br = broad.

losses that are likely due to removal of SbF_5 owing to thermal decomposition of SbF_6^-.[46] The residue of each sample was black and amorphous.

For comparison, $CuF_2(H_2O)_2(pyz)$ consists of 1D linear Cu−pyz−Cu chains; Cu-coordinated H_2O ligands are involved in strong hydrogen-bonding interactions of the Cu−F···H−O−Cu type, where the Cu···Cu and average F···O distances are 5.116 and 2.611 Å, respectively. While the F···O distance is ∼0.4 Å longer than the F···F distances found in **1a** and **1b**, each H-atom of the H_2O ligand in $CuF_2(H_2O)_2(pyz)$ is involved in hydrogen bond interactions. In spite of these subtle structural differences, the TGA results clearly indicate that the F···H−O hydrogen bonds found in $CuF_2(H_2O)_2(pyz)$ are much weaker than the F···H···F bonds found in **1a** and **1b** because decomposition and loss of H_2O ligands occur about 100 °C lower in temperature. These experimental results support the theoretical conclusion that the H···F hydrogen bonds in HF_2^- are stronger than the hydrogen bonds responsible for solid formation of water and hydrofluoric acid.

(46) Gantar, D.; Rahten, A. *J. Therm. Anal.* **1990**, *36*, 553.

5. Analysis of Vibrational Properties

Room temperature mid-IR spectra and peak assignments can be found in Figure 8 and Table 7, respectively. Common features of all three spectra are the combination of pyrazine ring stretching, in-plane bending, and C−H in-plane bending modes of medium intensity that occur between 1000 and 1200 cm^{-1}.[47] In addition, the medium-intensity peaks between 790 and 860 cm^{-1} are assigned to pyz C−H out-of-plane deformation modes. The symmetric and asymmetric C−H stretching modes of the pyz ligands appear as weak features between 3050 and 3180 cm^{-1}. Between 600 and 700 cm^{-1},[48] strong Sb−F stretching and F−Sb−F out-of-plane deformation modes occur as two peaks in **1a**, two peaks and two shoulders in **1b**, and a broad absorption in **2**. Relatively weak H···F hydrogen bond stretches overlap pyz C−H stretches but are observed as broad features

(47) Innes, K. K.; Byrne, J. P.; Ross, I. G. *J. Mol. Spectrosc.* **1967**, *22*, 125.

(48) Nakamoto, K. *Infrared and Raman Spectra of Inorganic and Coordination Compounds*, 5th ed.; John Wiley and Sons: New York, 1997.

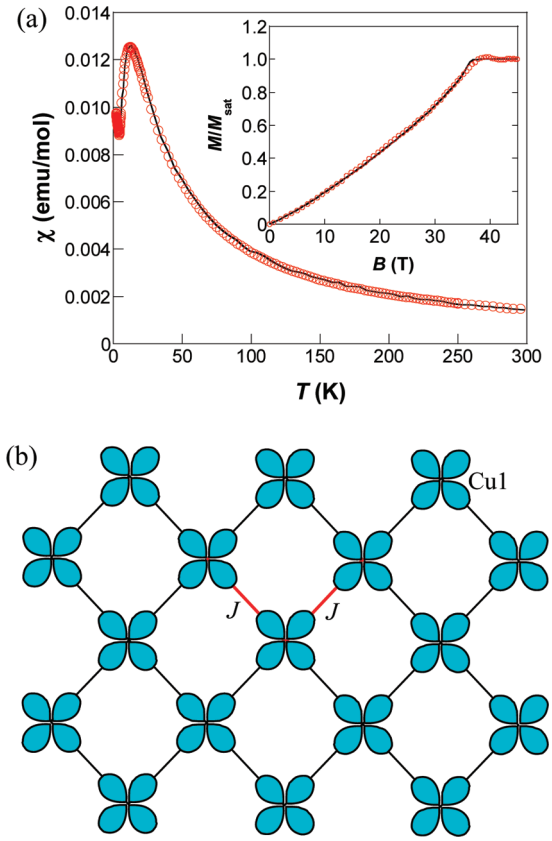

Figure 9. (a) Magnetic data for $[Cu(HF_2)(pyz)_2]SbF_6$ (**1a**): χ vs T obtained in a 0.1-T external field; (inset) measured $M(B)$ at 0.5 K. The solid lines in both plots are the results of QMC simulations as described in the text. (b) Arrangement of the magnetic $d_{x^2-y^2}$ orbitals forming the 2D square lattice in **1a**. The solid red lines denote the primary exchange path, J, while $J_\perp$ (not shown) represents the interlayer Cu−F···H···F−Cu exchange interaction.

above ~2800 cm^{-1}; in solid HF, the H···F hydrogen bonds yield modes between 3060 and 3420 cm^{-1}.[49−51]

Compounds **1a** and **1b** show additional broad absorptions between 1315 and 1625 cm^{-1} which are assigned to the asymmetric H···F bending mode;[49−51] **2** lacks this feature because the $H_3F_4^-$ molecule consists of more loosely bound H···F units, as evidenced by the crystallographic study that identified longer H···F bonds. The symmetric H···F stretch is expected to occur between 527 and 600 cm^{-1}, which is just beyond the range of our spectrometer.[49−51] Importantly, **1b** and **2** do not show evidence for the presence of H_2O, as the O−H bend would appear between 1600 and 1630 cm^{-1}.[48]

6. Analysis of the Magnetic Properties

6.1. Magnetic Susceptibility and Magnetization of $[Cu(HF_2)(pyz)_2]SbF_6$ (1a). χ vs $T$is shown in the main plot of Figure 9a, which displays a broad maxima at 12.5 K compared to 5.5 K observed for $[Cu(HF_2)(pyz)_2]BF_4$. Upon cooling below T_{max}, the susceptibility of **1a** decreases smoothly until 4.3 K, where it rises abruptly due to 3D magnetic ordering. The general shape of χ above and below the maximum is characteristic of the curves obtained for quasi-2D Heisenberg antiferromagnets.[39a,b,52−55] As an initial assessment of these data, a least-squares fit of χ vs T (in the region of $T \geq 40$ K) to a Curie−Weiss law was carried out, yielding $g = 2.143(1)$ and $\theta = -18.5(2)$ K, which indicates antiferromagnetic correlations between spin-1/2 Cu^{2+} ions. A plot of χT vs T for **1a** confirms the presence of dominant antiferromagnetic interactions, as evidenced by the continuous decrease between 300 and 2 K. Had the behavior below 4.3 K been due to a paramagnetic impurity, a temperature-independent response in χT vs T would have been anticipated.

Table 8. Comparison of Magnetic Parameters for Some Quasi-2D Pyrazine-Based Quantum Magnets Where the Cu−pyz−Cu Interaction Serves as the Primary Superexchange Pathway

compound	J (K)	T_N (K)	$\lvert k_BT_N/J\rvert$	$\lvert J_\perp/J\rvert$[a]	pyz tilt angle (°)[b]	references
1a	−13.4	4.31	0.32	9×10^{-3}	81.4	this work
1b	−3.81	1.7	0.44	3×10^{-1}	64.1	this work
$[Cu(HF_2)(pyz)_2]BF_4$	−5.7	1.54	0.27	9×10^{-4}	59.4	10, 57
$[Cu(HF_2)(pyz)_2]ClO_4$	−6.8	1.94	0.29	2×10^{-3}	64.2	57
$[Cu(HF_2)(pyz)_2]PF_6$	−12.6	4.31	0.34	1×10^{-2}	79.9	57
$[Cu(HF_2)(pyz)_2]AsF_6$	−13.0	4.34	0.33	1×10^{-2}	80.6	57
$[Cu(NO_3)(pyz)_2]PF_6$	−10.8	2.0	0.28	2×10^{-2}	61.4	68
$[Cu(NO_2)(pyz)_2]ClO_4$	−8.9	N/A[d]	N/A[d]	N/A[d]	59.7	40
$Cu(ClO_4)_2(pyz)_2$[c]	−17.7	4.21	0.24	8×10^{-4}	65.8	39a, 39c
$Cu(BF_4)_2(pyz)_2$[c]	−15.3	§3.5	0.23	7×10^{-2}	67.4	39a

[a] Calculated using eq 3 from ref 57 with the exception of **1b**, which was determined according to eq 8 of ref 71 that uses a modified random-phase approximation. [b] The listed pyrazine tilt angles correspond to room temperature crystal structures and were determined relative to the CuN_4 basal plane. [c] The corresponding structure contains parallel pyz rings along a Cu−pyz−Cu chain. [d] Not reported.

The magnetic interaction between Cu^{2+} ions is propagated by the σ-bond network through the μ-pyz ligands, although early work by Hatfield and co-workers proposed that the pyz π-system mediated the exchange interaction based on a molecular orbital study of $Cu(NO_3)_2(pyz)$ and $Cu(hfac)_2(pyz)$ (hfac = hexafluoroacetylacetonate).[56] The varying pyz tilt angles observed in these compounds were deemed responsible for the range of J-values. With the large number of structural data now available for quasi-2D systems, Table 8 reveals no universal trend in behavior. Compound **1a** shows the largest pyz tilt angle, and yet its J-value is lower than found for several examples that have smaller angles. However, for the family of $[Cu(HF_2)(pyz)_2]$-X compounds there is a qualitative trend between pyz tilt angle and T_N, where it can be seen that for octahedral X anions higher T_N values are attained. The most striking observation is that the tilt angles observed for $[Cu(HF_2)(pyz)_2]BF_4$ (59.4°) and $[Cu(NO_2)(pyz)_2]ClO_4$ (59.7°) are identical within experimental error; however, their J-values differ by ~40%. At present, we cannot explain the variation in J-values, although factors

(49) Azman, A.; Ocvirk, A.; Hadzi, D.; Giguere, P. A.; Schneider, M. *Can. J. Chem.* **1967**, *45*, 1347.
(50) Harmon, K. M.; Gennick, I. *J. Mol. Struct.* **1977**, *38*, 97.
(51) Gennick, I.; Harmon, K. M.; Potvin, M. M. *Inorg. Chem.* **1977**, *16*, 2033.
(52) Matsumoto, T.; Miyazaki, Y.; Albrecht, A. S.; Landee, C. P.; Turnbull, M. M.; Sorai, M. *J. Phys. Chem. B* **2000**, *104*, 9993.
(53) Woodward, F. M.; Albrecht, A. S.; Wynn, C. M.; Landee, C. P.; Turnbull, M. M. *Phys. Rev. B* **2002**, *65*, 144412. 5-MAP = 2-amino-5-methylpyridinium.
(54) Burriel, R.; Lambrecht, A.; Carlin, R. L. *J. Appl. Phys.* **1990**, *67*, 5853.
(55) Hammar, P.; Dender, D.; Reich, D.; Albrecht, A.; Landee, C. P. *J. Appl. Phys.* **1997**, *81*, 4615.
(56) (a) Richardson, H. W.; Hatfield, W. E. *J. Am. Chem. Soc.* **1976**, *98*, 835. (b) Richardson, H. W.; Wasson, J. R.; Hatfield, W. E. *Inorg. Chem.* **1977**, *16*, 484.

attributed to subtle distortion of the CuF_2N_4 octahedron and/or pyz rings, possibly induced by magnetoelastic effects, may be important.

For **1a** the isothermal magnetization, $M(B)$, measured at 0.5 K (Figure 9a, inset) rises slowly in low fields and then begins to rise more quickly as B is steadily increased. The fully polarized magnetic state is realized at $B_c = 37.6$ T. It should be mentioned that the general behavior of $M(B)$ is characteristic of quasi-2D spin-1/2 antiferromagnets owing to the concave nature of the curve for $0 \leq B < B_c$.[52−55] Importantly, measurements of $M(B)$ provide a rapid and independent determination of the spin dimensionality. Recently,[57] we carried out QMC simulations of the quantum-spin 2D Heisenberg square lattice with an additional interlayer exchange coupling energy, $J_\perp$, which quantitatively reproduces the data shown in the inset of Figure 9a. The degree of concavity depends on the effective spin dimensionality of the system, while the field, B_c, at which the "elbow" occurs (i.e., the fully polarized state) provides an accurate measure of the intralayer exchange energy in the limit $J \gg J_\perp$, where $J = gB_c/6.03$. Inserting $g = 2.14$ and $B_c = 37.6$ T into this equation leads to $J = 13.3$ K.

The χ vs T and $M(B)$ data for **1a** are well described by a spin-1/2 Heisenberg model based on an anisotropic cubic lattice:

$$H = -J\sum_{\langle i,j\rangle xy} S_i \cdot S_j - J_\perp \sum_{\langle i,j\rangle z} S_i \cdot S_j - h\sum_i S_i^z \qquad (1)$$

where J and $J_\perp$ are the strengths of the intra- and interlayer coupling constants, respectively. (Note that antiferromagnetic interactions are represented by negative J-values.) We have used the stochastic series expansion QMC method to study the above Hamiltonian for finite-sized lattices.[28−32] Excellent agreement with the experimental data of **1a** was achieved for $g = 2.14$, $J = -13.4$ K, and $J_\perp = -0.03J = -0.20$ K. The J-value obtained for **1a** is identical to the absolute value of 13.4 K calculated from the simple expression, $J = 1.07T_{max}$, derived explicitly for the Heisenberg 2D square lattice.[58] A calculated B_c of 37.7 T is obtained from the expression $(4J + 2J_\perp)/g\mu_B$ using the known g, J, and $J_\perp$ values. The square spin lattice for **1a** is illustrated in Figure 9b, highlighting the interaction of the magnetic $d_{x^2-y^2}$ orbitals.

The T_N/J ratio can be used to estimate the dimensionality of a magnetic system where ratios approaching unity reflect isotropic magnetic interactions. Combining $J = 13.4$ K with an assumed Néel temperature of 4.3 K, we calculate $T_N/J = 0.32$, which is less than that found for $(5\text{-MAP})_2CuBr_4$ (0.58)[53] but similar to those found for $Cu(ClO_4)_2(pyz)_2$ (0.24),[39a] $Cu(BF_4)_2$-$(py\text{-}O)_6$ (0.28),[59] and $[Cu(HF_2)(pyz)_2]BF_4$ (0.27).[10] Hence, it is likely that the HF_2^- bridge may contribute to the interlayer exchange mechanism, perhaps facilitated by a differential orbital overlap or mixing of the Cu $d_{x^2-y^2}$ and d_{z^2} wave functions.

6.2. Magnetic Susceptibility and Magnetization of $[Cu_2F(HF)(HF_2)(pyz)_4](SbF_6)_2$ (1b). Magnetic susceptibility data for **1b** measured in a static magnetic field of 0.1 T are shown in the main plot of Figure 10a. Although near the 2 K temperature limit of the SQUID magnetometer, a rounded maximum in χ vs T is clearly observed at 2.6 K, which is 10 K lower than the corresponding maximum found in **1a**. The difference in temperature where the maximum occurs suggests the presence of weaker magnetic interactions in **1b**. A fit of the reciprocal magnetic susceptibility to a Curie−Weiss law gave $g = 2.144(1)$ and $\theta = -1.9(1)$ K, which indicates a weaker antiferromagnetic interaction between spin-1/2 Cu ions compared to **1a**.

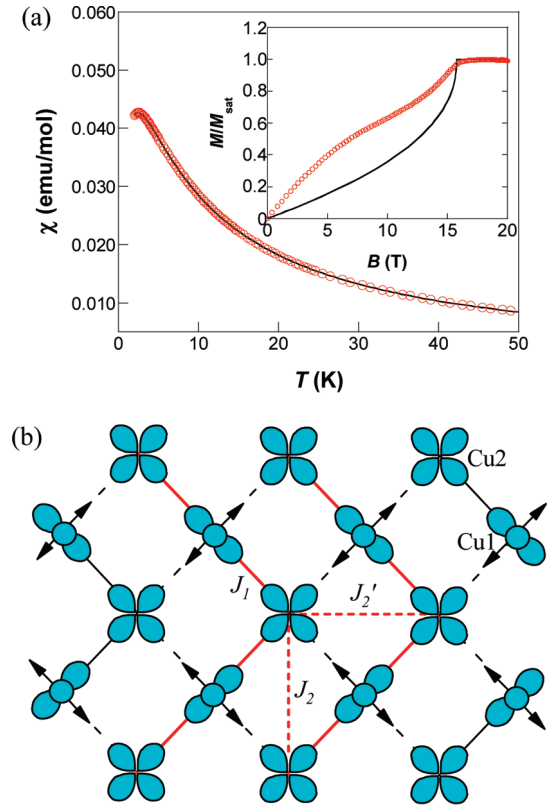

Figure 10. (a) Magnetic data for $[Cu_2F(HF)(HF_2)(pyz)_4](SbF_6)_2$ (**1b**): χ vs T obtained in a 0.1-T external field; (inset) measured $M(B)$ at 0.47 K and that calculated (solid line) using Griffiths' model for $T = 0$. (b) Intralayer arrangement of the $d_{x^2-y^2}$ magnetic orbitals in **1b**. Solid red lines denote primary exchange paths, while arrows and dashed red lines designate the Jahn−Teller axis (for Cu1) and interchain magnetic couplings, respectively. The Jahn−Teller axis of Cu2 is oriented normal to the layer.

The field-dependent magnetization, $M(B)$, measured at 0.47 K shows an unusual two-step saturation (Figure 10a, inset). These data are convex and resemble a Brillouin-like behavior until a step is reached at 10.8 T. Beyond this step, $M(B)$ becomes concave and rises abruptly until saturation is achieved at 15.8 T. It is interesting to note that the step occurs at two-thirds of the total magnetization, which is a behavior generally expected for frustrated spins on a triangular lattice or an ordered ferrimagnetic structure.[60] Since the structure of **1b** is based on a square lattice, spin frustration is probably not responsible for this behavior.

6.3. Cooperative Jahn−Teller Distortion (CJTD) and Spin Exchange Model for $[Cu_2F(HF)(HF_2)(pyz)_4](SbF_6)_2$ (1b). It is well known that d^9 ions such as Cu^{2+} are expected to undergo a Jahn−Teller distortion of typically the axial-elongation type to remove the degeneracy of the e_g orbitals ($d_{x^2-y^2}$ and d_{z^2}). The energy difference (Δe) between these two orbitals is affected

(57) Goddard, P. A.; Singleton, J.; Sengupta, P.; McDonald, R. D.; Lancaster, T.; Blundell, S. J.; Pratt, F. L.; Cox, S.; Harrison, N.; Manson, J. L.; Southerland, H. I.; Schlueter, J. A. *New J. Phys.* **2008**, *10*, 083025.
(58) Takahashi, M. *Phys. Rev. B* **1989**, *40*, 2494.
(59) Algra, H.; de Jongh, L. J.; Carlin, R. L. *Physica B* **1978**, *93*, 24. py-O = pyridine-*N*-oxide.
(60) Richter, J.; Schulenburg, J.; Honecker, A. In *Quantum Magnetism in Two Dimensions: From Semi-classical Néel Order to Magnetic Disorder*, Lecture Notes in Physics, Vol. 645; Schollwöck, U., Richter, J., Farnell, D. J. J., Bishop, R. F., Eds.; Springer: Berlin, 2004.

by the degree of distortion. For **1a**, this distortion occurs uniformly along the Cu−F···H···F−Cu direction, i.e., perpendicular to the layers, a feature typical of other layered structures such as $Cu(ClO_4)_2(pyz)_2$, which is described as a ferrodistortion (FD). The presence of broken HF_2^- links in **1b** increases the entropy of the system by providing a less robust 3D framework that can accommodate a CJTD, thus leading to two crystallographically unique Cu^{2+} sites that exhibit $d_{x^2-y^2}$ orbital ordering.

Alternation of the Jahn−Teller axes within a layer leads to an antiferrodistortive (AFD) arrangement, thus causing the magnetic interaction to be highly anisotropic for **1b**. In contrast, **1a** adopts an isotropic 2D square spin lattice (Figure 9b). The alternation of Jahn−Teller axes produces inequivalent Cu···Cu distances of 6.909 and 7.174 Å within a layer. From Figure 10b, it can be seen that, for the Cu1 sites, two lobes of the $d_{x^2-y^2}$ magnetic orbital are projected normal to the 2D layer, while the other two lobes lie in the layer. This particular arrangement effectively reduces the spin dimensionality of the system to one (*a priori*). All four lobes of the $d_{x^2-y^2}$ magnetic orbital for the Cu2 sites occupy the *bc*-plane. The in-plane distribution of exchange couplings is consistent with orthogonal zigzag chains propagating along the *c*-direction, while weaker interchain interactions along the *a*- and *b*-axes must also be considered. Hence, **1b** is described as quasi-1D compared to **1a**, which is quasi-2D. The "quasi" descriptor is used here to emphasize that no real material is perfectly 1D or 2D and that additional interactions are necessary to account for interchain or interlayer couplings. The orbital ordering exhibited by **1b** is unique and persists over the temperature range (90−295 K) studied by X-ray diffraction. In another quasi-2D compound, single crystals of $Cu(ClO_4)_2(py\text{-}O)_6$ prepared from an acetonitrile solution show an AFD ordering below 60 K.[61]

In accord with Figure 10b, the magnetic susceptibility data for **1b** were fitted between 2 and 50 K to a 1D quantum Heisenberg uniform chain model ($H = -J\sum S_i \cdot S_{i+1}$) as formulated by Johnston et al. (eq 2) based on the traditional thermodynamic Bethe ansatz.[62]

$$\chi = \frac{C}{T}\frac{1+\sum_{n=1}^{q} N_n/t^n}{1+\sum_{n=1}^{r} D_n/t^n} \qquad (2)$$

In eq 2, C is the Curie constant, $t = T/J$, and D_n and N_n are the coefficients found in Table 9. In order to account for the interchain magnetic couplings J_2 and J_2' (which are approximately equivalent), a mean-field correction term (that considers the number of magnetic nearest neighbors, z) was included in the expression. The solid curve shown in the main plot of Figure 10a is the result of the best least-squares fit, which yields $g = 2.127(1)$, $J_1 = -3.81(1)$ K, and $zJ_2 = zJ_2' = -0.48(1)$ K. The absolute value of J_1 is in good agreement with the expected value of 3.98 K obtained from the relation $J = 1.560k_BT_{max}$ expected for a spin-1/2 Heisenberg 1D chain.[62] Within a layer, there are two magnetic nearest-neighboring chains and two additional chains in adjacent layers, thus giving a total $z = 4$. Hence, the values of J_2 and J_2' are −0.12 K, which is ∼3% of the magnitude of J_1.

Table 9. Johnston's Coefficients of Eq 2 for the Magnetic Susceptibility of the Quantum-Spin Heisenberg Antiferromagnetic Chain

n	N_n	D_n
1	−0.053837836	0.44616216
2	0.097401365	0.32048245
3	0.014467437	0.13304199
4	0.0013925193	0.037184126
5	0.00011393434	0.0028136088
6	0	0.00026467628

Our DFT calculations on **1b** using the B3LYP functional and the 6-31G* basis set for the BS and HS states of the spin-dimer units representing J_1, J_2, and J_2' led to the results $J_1 = -12$ K, $J_2 = -0.2$ K, and $J_2' = -0.1$ K, which qualitatively agrees with our spin exchange model. However, as shown in the inset of Figure 10a, the simulation of the $M(B)$ data using this model resulted in poor agreement; $M(B)$ would be strongly concave and closely resemble the magnetization of the 1D spin-1/2 chain model calculated by Griffiths (solid line in the inset of Figure 10a).[63] Hence, a spin Hamiltonian with additional spin exchange interactions (i.e., weak interlayer ferromagnetism) may be necessary to simulate the $M(B)$ data and specifically the inflection that occurs at two-thirds of M_{sat}.

Let us now consider possible interlayer exchange pathways in **1b**. Assuming the crystal structure does not change drastically and the aforementioned orbital ordering persists to low temperatures, the unpaired electrons in Cu1 and Cu2 remain in the $d_{x^2-y^2}$ orbitals. In Figure 11a we propose an exchange path that requires interaction between F11 (from a SbF_6^- ion) and the HF ligand coordinated to Cu1. The net result is an interlayer Cu1−F2−H2···F11···H2−F2−Cu1 hydrogen bond [H2···F11 = 1.728 Å, F2−H2···F11 = 175.8° at 295 K]. Because of symmetry, this interlayer link alternately staggers from one layer to the next. If a spin polarization mechanism is operative, the bulk of the spin density would be localized on copper and fluorine atoms in a manner such as Cu(↑)−F(↓)−H···F(↑)···H−F(↓)−Cu(↑), which leads to a ferromagnetic coupling between Cu sites. This also implies a minimal spin density on the intervening H atoms; should the H-atoms play a significant role in this mechanism, a ferromagnetic interaction would be inevitable. This is in contrast to any possible magnetic interaction along the bifluoride bridge since an antiferromagnetic coupling of the type Cu2(↑)−F3(↓)···H3···F3A(↑)−Cu2(↓) is predicted, which is consistent with DFT results obtained for $[Cu(HF_2)(pyz)_2]BF_4$, where the HF_2^- F-atoms were found to possess a small spin density of 0.001 μ_B.[64]

We also note that a pyz(H)···F (∼2.5 Å) interaction may also facilitate a secondary, albeit weak, interlayer exchange interaction in both **1a** and **1b**. The larger SbF_6^- counterion is approximately twice as large as BF_4^-, suggesting an enhanced magnetic interaction between the pyz H-atoms and peripheral F-atoms in the former. A somewhat longer interaction (3.0 Å) across an edge-to-edge diagonal (i.e., H···F−Sb−F···H) may also be important, as every proton in an HF_2^- bridge is involved in four such interactions. The more complex H···F hydrogen-bonding found in **1b** leads to more complex magnetic behavior.

(61) (a) Wood, J. S.; Keijzers, C. P.; de Boer, E.; Buttafava, A. *Inorg. Chem.* **1980**, *19*, 2213. (b) O'Connor, C. J.; Sinn, E.; Carlin, R. L. *Inorg. Chem.* **1977**, *16*, 3314.

(62) (a) Johnston, D. C.; Kremer, R. K.; Troyer, M.; Wang, X.; Klümper, A.; Bud'ko, S. L.; Panchula, A. F.; Canfield, P. C. *Phys. Rev. B* **2000**, *61*, 9558. (b) Klumper, A.; Johnston, D. C. *Phys. Rev. Lett.* **2000**, *84*, 4701.

(63) Griffiths, R. B. *Phys. Rev. A* **1964**, *133*, A768.

(64) Middlemiss, D. S.; Lawton, L. M.; Morrison, C. A.; Wilson, C. *Chem. Phys. Lett.* **2008**, *459*, 119.

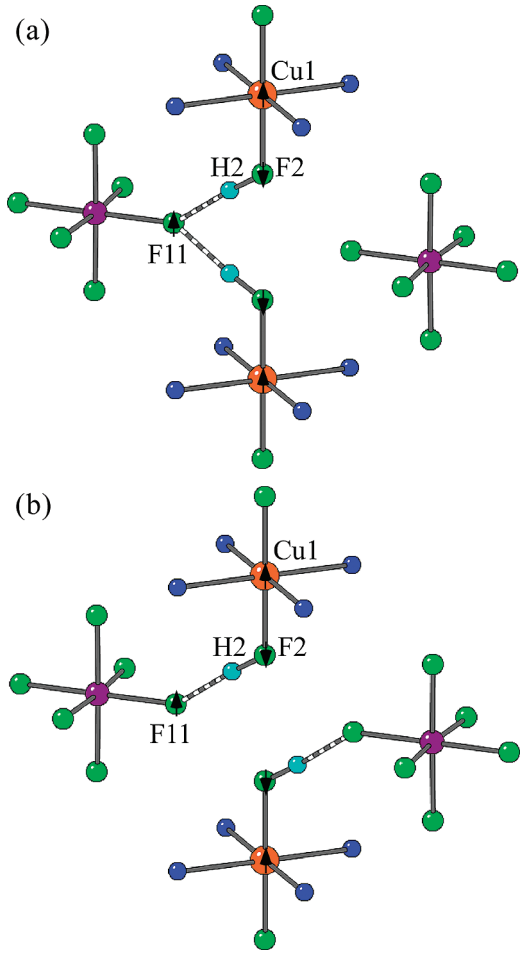

Figure 11. (a) Illustration of the interlayer exchange pathway proposed for **1b** assuming that the HF protons are directed toward a common F. (b) Alternatively, the H2's could point toward different F11's to produce essentially no exchange interaction. Arrows denote the sign of the spin polarization on the Cu and F atoms involved in the superexchange.

6.4. Magnetic Susceptibility and Magnetization of [CuAg(H$_3$F$_4$)(pyz)$_5$](SbF$_6$)$_2$ (2). The main plot of Figure 12a shows the magnetic susceptibility data for **2** between 2 and 50 K. The susceptibility gradually increases as the temperature is lowered to 2 K, with no evidence for short- or long-range spin correlations over the entire T-range. Using a Curie−Weiss law to ascertain the Weiss constant, we obtain $g = 2.141(1)$ and $\theta = -0.01(1)$ K, which indicates the usual anisotropy in the g-tensor and negligible exchange interactions between Cu^{2+} ions.

The weak nature of the magnetic coupling in **2** can be rationalized by considering the probable $d_{x^2-y^2}$ orbital interactions as depicted in Figure 12b. Based on evaluation of the crystal structure, the Jahn−Teller axis lies along the a-axis and contains the nonmagnetic d_{z^2} orbital which leads to a negligible exchange path. This leaves two possible exchange pathways: (1) Cu−F···H···F···H···F−Cu in which the Cu···Cu distance is 7.7947(4) Å or (2) Cu−pyz−Ag−pyz−Cu where the Cu···Cu separation is considerably longer at 14.7562(6) Å. In the latter scenario, the through-bond superexchange interaction not only involves a large distance but also entails an intervening diamagnetic Ag^+ ion.

The $M(B)$ curve obtained for **2** using a SQUID magnetometer (Figure 12a, inset) is well reproduced by the Brillouin function[65]

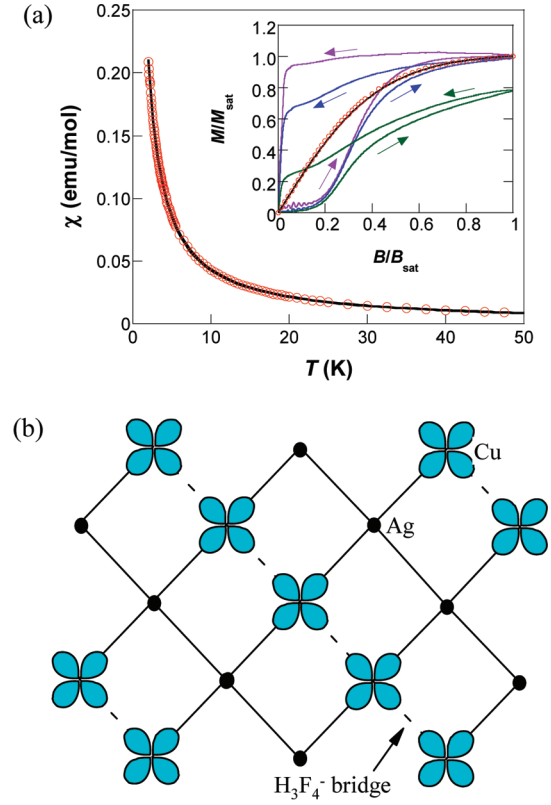

Figure 12. (a) χ vs T for **2** obtained in a 0.1-T magnetic field. The solid line is a theoretical fit of the data to a Curie−Weiss law as described in the text. (Inset) Pulsed-field $M(B)$ data for **2** measured at 0.4 (purple), 1.5 (blue), and 4.3 K (green) along with 2 K SQUID data (○) and calculated (black line) Brillouin magnetization for $g = 2.15$ and $\theta = 0$. Arrows indicate the sweep direction of the pulsed field. (b) Arrangement of $d_{x^2-y^2}$ magnetic orbitals in a layer of **2**. The Cu Jahn−Teller axis lies perpendicular to the layer.

for isolated quantum spins based on a g-factor of 2.15. More unusual results were obtained when **2** was placed in a pulsed magnetic field. For the three temperatures measured, the magnetization is clearly irreversible and displays substantial hysteresis. The observed hysteresis is atypical of the majority of magnetic materials in that the hysteresis occurs between the up and down sweeps and is unlikely to be the result of conventional magnetic order (i.e., ferromagnetism). From the data in hand, an unusually slow relaxation of the spin system and/or magnetocaloric effect[66] may be operative, a possible consequence of the different hydrogen bond motif observed in **2** as compared to those of **1a** and **1b**. While these results are intriguing, further investigation is warranted which is beyond the scope of the present work.

6.5. Long-Range Magnetic Order in [Cu(HF$_2$)(pyz)$_2$]SbF$_6$ (1a) and [Cu$_2$F(HF)(HF$_2$)(pyz)$_4$](SbF$_6$)$_2$ (1b). 6.5.1. Zero-Field (ZF) Muon-Spin Relaxation. In order to confirm LRO in **1a** and search for LRO in **1b**, muon-spin relaxation (μ^+SR) measurements were conducted at ISIS and PSI, respectively. At the base temperature, clear oscillations in the muon asymmetry function, $A(t)$, were observed for both **1a** and **1b** due to coherent precession of the muon-spin ensemble (Figure 13a).[27] The form of the μSR spectra led us to believe that **1a** and **1b** are completely ordered throughout their bulk below their respective T_N's. Oscillations at two distinct frequencies, ν_i, were

(65) Kahn, O. *Molecular Magnetism*; VCH Publishers: Weinheim, 1993.

(66) Tishin, A. M.; Spichkin, Y. I. *The Magnetocaloric Effect and its Applications*; IoP Publishers: Bristol, 2003.

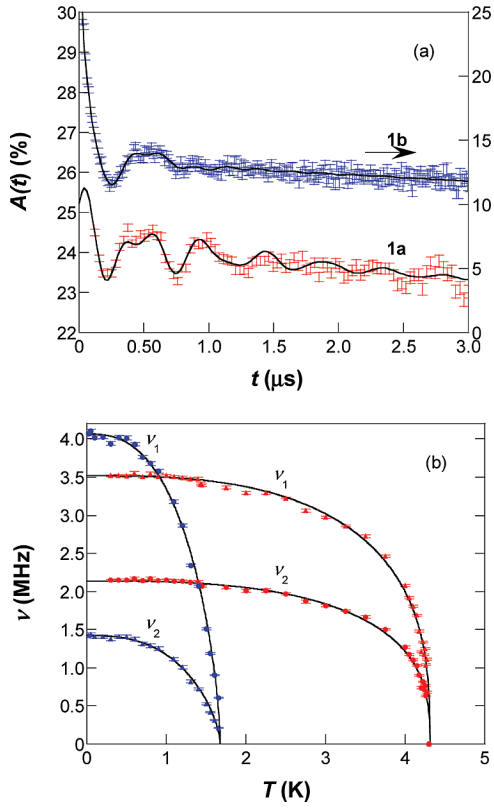

Figure 13. (a) ZF asymmetry spectra obtained at 0.3 and 0.02 K for **1a** (red) and **1b** (blue), respectively. (b) *T*-evolution of the muon precession frequencies, ν, for **1a** and **1b**. Compound **1a** has the higher T_N.

obtained from the $A(t)$ spectra below T_N suggesting the existence of two magnetically unique muon stopping sites. By monitoring this behavior as a function of temperature, an effective order parameter can be obtained (Figure 13b) from power law fits of the form $\nu_i(T) = \nu_i(0)[1 - (T/T_N)^{\alpha}]^{\beta}$, where $\nu_1(0) = 3.52$ MHz, $\nu_2(0) = 2.14$ MHz, $\alpha = 2.8(1)$, and $\beta = 0.34(1)$ for **1a** and $\nu_1(0) = 4.04$ MHz, $\nu_2(0) = 1.42$ MHz, $\alpha = 3.3(2)$, and $\beta = 0.33(2)$ for **1b**. The point at which these oscillations vanish is the Néel temperature, T_N, which was determined to be 4.31(1) and 1.7(1) K for **1a** and **1b**, respectively. The β-values of both materials are consistent with that expected for a 3D Heisenberg antiferromagnet ($\beta = 0.367$).[67] In the paramagnetic regime above T_N, these rapid oscillations cease, and much broader oscillations appear due to a μ^+-F nuclear dipole interaction as described in previous work.[68]

6.5.2. Heat Capacity. Temperature-dependent heat capacity studies, $C_p(T)$, on **1a** and **1b** carried out in zero-field are presented as $C_p(T)/T$ vs T plots in the insets of Figure 14a and b, respectively. For **1a** and **1b**, λ-anomalies observed at ~4.2 and 1.7 K, respectively, are attributed to long-range spin ordering (T_N). As the temperature increases, $C_p(T)$ rises quickly due to the lattice contribution to the heat capacity. It is recalled that the total measured heat capacity represents the sum of the lattice (C_{latt}), electronic (C_{elec}), and magnetic (C_{mag}) contributions. The former and latter are important at high and low temperatures, respectively, whereas C_{elec} is negligible in these insulating materials. With the aim of obtaining a good estimate of C_{mag}, we must determine and subtract the appropriate amount of C_{latt}.

In order to model the lattice contribution, C_{latt} (solid lines in Figure 14 insets), we used eq 3 considering one Debye mode and two Einstein modes,

$$C_{latt} = \frac{3A_D}{x_D^3}\int_0^{x_D}\frac{x^4 e^x}{(e^x-1)^2} + A_{E1}\frac{\theta_{E1}^2}{T^2}\frac{e^{(\theta_{E1}/T)}}{[e^{(\theta_{E1}/T)}-1]^2} + A_{E2}\frac{\theta_{E2}^2}{T^2}\frac{e^{(\theta_{E2}/T)}}{[e^{(\theta_{E2}/T)}-1]^2} \quad (3)$$

where $x = \hbar\omega/k_BT$, and the subscripts D and E denote Debye and Einstein terms, respectively. The parameters obtained from the least-squares fitting routine are given in Table 10.

The Debye term was integrated numerically using 2000 mesh points. For **1b** no evidence of short-range magnetic order above T_N was observed, and the data were fitted to eq 3 above 10 K. In **1a** the magnetic entropy associated with short-range spin correlations is significant, and we described this behavior in terms of the polynomial expression given in ref 39c, based on the QMC simulations of ref 69. Those simulations suggest that the heat capacity associated with the long-range ordering will be quite small for temperatures

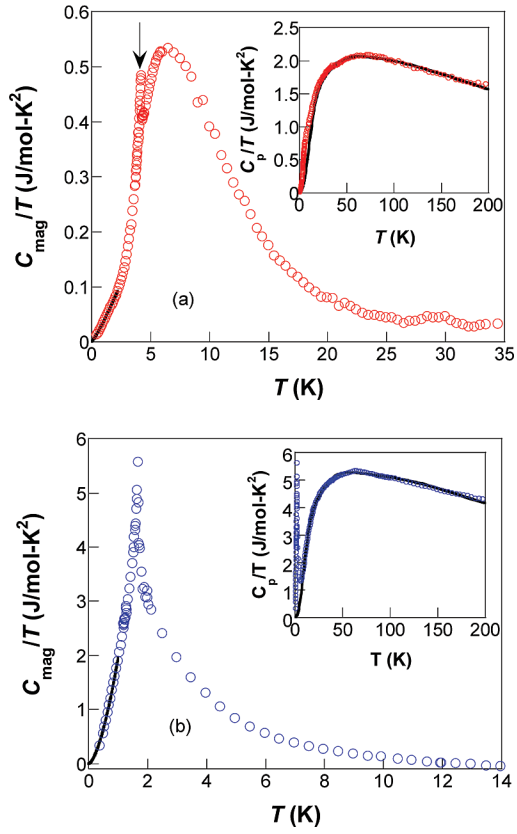

Figure 14. C_{mag}/T vs T for (a) $[Cu(HF_2)(pyz)_2]SbF_6$ (**1a**) and (b) $[Cu_2F(HF)(HF_2)(pyz)_4](SbF_6)_2$ (**1b**). The solid lines for $T < T_N$ are fits to a spin wave model as described in the text. (Inset) C_p/T vs T for **1a** and **1b**; solid lines represent the calculated lattice heat capacity, C_{latt}, as determined by fitting the data to eq 3.

Table 10. Parameters of the Lattice Modes Derived from Analysis of the Zero-Field Heat Capacity Data for $[Cu(HF_2)(pyz)_2]SbF_6$ (**1a**) and $[Cu_2F(HF)(HF_2)(pyz)_4](SbF_6)_2$ (**1b**) As Described in the Text

parameter	$[Cu(HF_2)(pyz)_2]SbF_6$ (**1a**)	$[Cu_2F(HF)(HF_2)(pyz)_4](SbF_6)_2$ (**1b**)
A_D (J/mol-K)	76(1)	162(2)
A_{E1} (J/mol-K)	134(4)	332(7)
A_{E2} (J/mol-K)	191(4)	587(11)
θ_D (K)	94.3(8)	83.5(6)
θ_{E1} (K)	208(4)	185(3)
θ_{E2} (K)	500(13)	500(10)

just above T_N in our system. We therefore fitted the sum of this polynomial and eq 3 to the data of **1a** for $T > 6$ K, i.e., above T_N.

The magnetic contributions to the heat capacities, C_{mag}, are shown in the main panels of Figure 14. In **1a**, there is a broad peak at 6.7 K owing to short-range spin correlations which is the dominant feature of C_{mag}, while the λ-anomaly at ~4.2 K signifies the crossover from 2- to 3D magnetic ordering. The total magnetic entropy is 6 J/mol-K (~$1.04R \ln 2$), which considers one unique Cu^{2+} ion per formula unit in **1a** within the expected 5% error of the calorimeter. From the T_{max} of the broad feature in C_{mag} we estimate the magnetic exchange constant within the 2D $[Cu(pyz)_2]^{2+}$ layers to be 13.0(5) K. The precise value depends on the assumptions made in the analysis and is further complicated by the magnetic ordering. Around 85% of the magnetic entropy appears above T_N, consistent with the low dimensionality evident in other techniques. In **1b**, the λ-anomaly at 1.7 K is quite large compared to that observed for **1a**, and while there are no distinct magnetic features attributable to short-range magnetic order, more than half of the magnetic entropy appears above T_N, showing that the exchange interactions remain anisotropic. The total magnetic entropy derived from these contributions is 11.5 J/mol-K (~$2R \ln 2$), as expected for two unique Cu^{2+} ($S = 1/2$) ions per formula unit.

The magnitude of the observed λ-anomalies displayed by **1a** and **1b** is important and warrants further discussion. As pointed out by Sengupta et al.,[69] the presence of interlayer interactions, $J_\perp$, induces a transition to long-range order, thus causing a local maximum in the heat capacity at T_N. This maximum becomes undetectably small for ratios $J_\perp/J < 0.01$ but grows rapidly as the ratio increases. The fact that we observe significant λ-peaks implies substantial interlayer couplings in **1a** and **1b**. From the QMC simulation of the magnetic susceptibility and magnetization data for **1a**, $J_\perp/J$ was determined to be 0.03, which exceeds the threshold of 0.01. Because $J_\perp/J > 0.01$, we should expect to observe a λ-anomaly in the case of **1a**, as has been confirmed. For **1b** the λ-anomaly is much larger than for **1a**, which indicates that the exchange interactions are more isotropic. Comparing the data for **1b** to the model in ref 69 suggests that the interlayer coupling is ~40% of J_1, but this is a significant oversimplification and is incompatible with the form of the magnetic susceptibility and magnetization (Figure 10a). Instead, a more complicated interplay of exchange interactions is required to satisfactorily describe all the data.

For $T \ll T_N$, a simple spin wave model, $C_{SW} \sim T^{d/n}$,[70] can be used to evaluate the spin dimensionality of the system in the magnetically ordered state; $n = 1$ (antiferromagnetic spin waves) or $n = 2$ (ferromagnetic spin waves). Assuming $n = 1$, fits of the data presented in Figure 14 to this model yielded $d = 2.17(1)$ and 2.61(3) for **1a** and **1b**, respectively. These values of d suggest the presence of significant 2D correlations in **1a**, while **1b** is better approximated by a T^3 dependence as expected for a 3D antiferromagnet. We found the d-value to vary by ~1% depending on the temperature range used in the fit; however, the model is only valid for $T \ll T_N$. Knowing T_N and J for **1b**, we obtain a T_N/J ratio of 0.44, which is larger than that calculated for **1a**. This result agrees with the spin wave model and also confirms the higher spin dimensionality of **1b** as compared to **1a**.

7. Concluding Remarks

We have explored the potential of strong H···F hydrogen bonds to act as ligands in the self-assembly of novel quantum magnetic solids. Three such compounds, $[Cu(HF_2)(pyz)_2]SbF_6$ (**1a**), a second polymorph $[Cu_2F(HF)(HF_2)(pyz)_4](SbF_6)_2$ (**1b**), and $[CuAg(H_3F_4)(pyz)_5](SbF_6)_2$ (**2**), have been prepared from aqueous solution using HF_2^- as a synthon. Because HF_2^- is coordinated to the Jahn−Teller axis of the Cu^{2+} ion in all three compounds, the observed magnetic interaction between the Cu^{2+} ions through the HF_2^- is predictably weak. While the observed H···F bonds of HF_2^- in **1a** and **1b** appear to be symmetric on the basis of X-ray structural evidence, it is unclear whether the symmetry of the HF_2^- is influenced by electronic effects or crystal packing or a combination thereof. Neutron diffraction data are needed to precisely locate the H-atoms of the HF adducts present in **1a**, **1b**, and **2**, and these efforts are in progress. The present work demonstrates the need for complementary theoretical models and simulations to properly describe the experimental data provided by several magnetic probes. The differing H···F hydrogen-bonding schemes encountered in **1a**, **1b**, and **2** create varying complexities in the probable exchange pathways and spin dimensionalities. In order to better evaluate the superexchange efficiency of strong H···F bonds, it is necessary to synthesize other analogues that contain Mn^{2+}, Fe^{2+}, Co^{2+}, and Ni^{2+} ions. A major synthetic effort is underway to develop a wide variety of coordination complexes that contain H···F adducts.

Acknowledgment. Work at EWU was supported by an award from Research Corporation. The Bruker (Siemens) SMART APEX diffraction facility was established at the University of Idaho with the assistance of the NSF-EPSCoR program and the M. J. Murdock Charitable Trust, Vancouver, WA. Work was supported by UChicago Argonne, LLC, operator of Argonne National Laboratory ("Argonne"). Argonne, a U.S. Department of Energy (DoE) Office of Science Laboratory, is operated under contract no. DE-AC02-06CH11357. Research performed at North Carolina State University was supported by the Office of Basic Energy Sciences (BES), Division of Materials Sciences of the U.S. DoE under Grant No. DE-FG02-86ER45259. T.L., P.A.G., and S.C. gratefully acknowledge, in order, support from the Royal Commission for the Exhibition of 1851, the Glasstone Foundation, and the Seaborg Institute (LANL). This work was also supported by the EPSRC, UK. Work at the NHMFL was conduced under the auspices of the National Science Foundation, the DoE BES program "Science in 100 T", and the State of Florida.

Supporting Information Available: X-ray crystallographic files in CIF format for compounds **1a**, **1b**, **2**, and $Cu(pyz)_2(SbF_6)$. ORTEP drawing, atom labeling scheme, and packing diagram for $Cu(pyz)_2(SbF_6)$; complete ref 35. This material is available free of charge via the Internet at http://pubs.acs.org.

JA808761D

(67) Talapov, A. L.; Blöte, H. W. J. *J. Phys. A* **1996**, *29*, 5727.
(68) Lancaster, T.; Blundell, S. J.; Baker, P. J.; Brooks, M. L.; Hayes, W.; Pratt, F. L.; Manson, J. L.; Conner, M. M.; Schlueter, J. A. *Phys. Rev. Lett.* **2007**, *99*, 267601.
(69) Sengupta, P.; Sandvik, A. W.; Singh, R. R. P. *Phys. Rev. B* **2003**, *68*, 094423.
(70) Miedema, A. R.; de Jongh, L. J. *Adv. Phys.* **1974**, *23*, 1.
(71) Yasuda, C.; Todo, S.; Hukushima, K.; Alet, F.; Keller, M.; Troyer, M.; Takayama, J. *Phys. Rev. Lett.* **2005**, *94*, 217201.